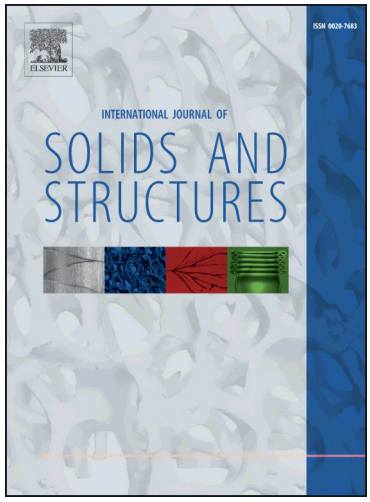

A computational model for large deformations of composites with a 2D soft matrix and 1D anticracks

Ettore Barbieri, Nicola Maria Pugno

PII: S0020-7683(15)00363-7
DOI: http://dx.doi.org/10.1016/j.ijsolstr.2015.08.015
Reference: SAS 8880

To appear in: *International Journal of Solids and Structures*

Received Date: 18 August 2014
Revised Date: 15 August 2015

Please cite this article as: Barbieri, E., Pugno, N.M., A computational model for large deformations of composites with a 2D soft matrix and 1D anticracks, *International Journal of Solids and Structures* (2015), doi: http://dx.doi.org/10.1016/j.ijsolstr.2015.08.015

A computational model for large deformations of composites with a 2D soft matrix and 1D anticracks

Ettore Barbieri[c,*], Nicola Maria Pugno[a,b,c]

[a] *Laboratory of Bio-Inspired and Graphene Nanomechanics, Department of Civil, Environmental and Mechanical Engineering, University of Trento, Via Mesiano 77, I-38123 Trento, Italy*
[b] *Centre for Materials and Microsystems, Fondazione Bruno Kessler, Via Sommarive 18, I-38123 Povo (Trento), Italy*
[c] *School of Engineering and Materials Science, Queen Mary University of London, Mile End Road, E1 4NS, London, UK*

Abstract

Anticracks (also known as Rigid Line Inclusions) occur frequently in a variety of natural and engineered composites as very stiff and extremely sharp (almost zero-thickness) fibres or lamellae embedded in a softer matrix.

In the linear elastic regime, similarly to cracks, anticracks generate a singularity in the stress distribution around the tip. Because of this similarity, existing analytical techniques and solutions (for simple cases) can be easily translated to anticracks. However, despite their importance in many biological and engineering composites, there has been surprisingly little development of numerical methods that would account simultaneously for the presence of multiple fibres or lamellae, arbitrary loadings and nonlinear behaviour of the matrix.

This paper presents the first numerical approach for rigid line inclusions, based on a meshfree scheme recently developed for multiple crack growth in elastic media. The inclusion of zero thickness is created as a crack, and a rigid motion (rotation and translation) is enforced at the anticrack faces. The equations of motion are solved according to a Total Lagrangian framework, and the matrix supposed hyperelastic.

Contrarily to available analytical solutions, the degrees of freedom of the rigid motion are determined *a posteriori* as a consequence of the (discretized) elastic equilibrium, expressed in a variational approach.

Results show that the proposed approach match well the analytical solutions and provides accurate Stress Intensity Factors (SIFs) for relatively little computational cost. Moreover, the method can reproduce some peculiar features of the anticracks: unlike cracks, singularities also appear under compressive and parallel loads; moreover, for a certain combination of biaxial load, stress concentrations disappear.

Finally, the paper presents examples drawn from biological and engineering composites: the reorientation of one or more fibres under large strains, resulting in a smart stiffening and strengthening mechanism. Reorienting towards the direction of applied load has structural importance since reinforcements can have the most effectiveness in withstanding loads. If the matrix is compliant, the reorientation is eased.

Keywords:
anticracks, rigid line inclusions, lamellae, needles, fibres, platelets, fibre reorientation

1. Introduction

A Rigid Line Inclusion (RLI) is a mathematical abstraction of an extremely thin stiff inclusion dispersed within a matrix. The definition assumes the inclusion as infinitely rigid and *zero-thickness*. Kinematically, this model consists in a surface of discontinuity (a crack) where a rigid motion is imposed on all the material points belonging to the upper and lower faces of the inclusion. For this reason, some authors (Hurtado et al., 1996) refer to this model as an *anticrack*. However, in geology this terminology indicates something different: a classical Mode I crack displacement solution with a reversed sign (Fletcher and Pollard, 1981), which in classical fracture mechanics means a violation of the non-penetrability of the crack faces. However, the justification is the dissolution and removal of material when the anticrack surfaces move toward each other, which is useful to explain triggering mechanism for snow slab avalanches (Heierli et al., 2008) or shallow earthquakes (Green et al., 1990; Burnley and Green, 1989). In RLI instead, the impenetrability is automatically imposed by a rigid motion common to both faces.

RLIs are useful to model the effects on the matrix of thin reinforcements in form of fibres, platelets, needles or rods of characteristic sizes much smaller than that of the embedding matrix. These reinforcements appear in many biological systems and engineered nanocomposites. For example, in biological systems (Pingle et al., 2008) like bones, teeth or nacre, the reinforcement is usually in mineralized crystal form arranged in a *staggered* disposition within a protein matrix. In calcified tissues, (Landis, 1995), these fibres influence their strength, and the overall effect is a tough nanocomposite (Ji and Gao, 2004) produced from very *poor* materials (Fratzl and Guille, 2011). In engineered nanocomposites, RLIs appear as needle-like reinforcements (Bilotti et al., 2008, 2009, 2010), nanowhiskers (Eichhorn et al., 2010), nanoplatelets (Porwal et al., 2013b,a,c) and carbon nanotubes (Nishimura and Liu, 2004).

Many theoretical papers are available in the literature for the RLI problem, often encountered with different terminology, such as *line stiffener* or *anticrack*, owed to its resemblance with a crack. Most likely, this abundance is due to the application to RLI of already well-known techniques at that time for 2D problems: for instance, the Mushkelishvili solutions in terms of complex variable, and the Wiener-Hopf technique, previously applied for crack problems (Muskhelishvili, 1953).

Probably the first paper on RLI appeared in 1973 (Atkinson, 1973), with the term *ribbon* instead of *rigid line inclusion*. The scope of this paper was to study the response of a metallic strain measuring device in a rubber matrix. This paper presented firstly the solution for stresses in an elastic linear matrix due to a single isolated rigid *ribbon*, and secondly the solution for the *elastic ribbon*. The crack analogy is then exploited to obtain the solution for two collinear rigid inclusions, and finally, the interaction of a RLI with a free boundary. Later, (Brussat and Westmann, 1975) proved the correspondence between the *Westergaard* stress function for cracks and a stress function for RLI, and subsequently, the relation between their *Stress Intensity Factors* (SIFs). (Hasebe et al., 1984) instead proposed a rational mapping function (again taken from the elasticity of cracks) to analyse the stress state near a the tip of a crack

*Corresponding author
Email addresses: e.barbieri@qmul.ac.uk (Ettore Barbieri), Nicola.Pugno@unitn.it (Nicola Maria Pugno)

initiated from the tip of a RLI. (Wang et al., 1985) obtained the asymptotic expansion near the tip of a RLI (reported in section 2.2 of this paper) for both stress and and strain fields. (Chen, 1986) and later (Stagni, 1989) proved the path-independence of the *J-integral* around the tip of a RLI, and found that the *J-integral* for an anticrack is negative, rather than positive like in cracks. (Dundurs and Markenscoff, 1989) and (Ballarini, 1987) reported a *full-field* solution for the stresses in the matrix due to a RLI, respectively using a *weight function technique* and an *integral equation approach*, and later for a RLI at the interface of two dissimilar materials (Ballarini, 1990). (Hurtado et al., 1996) introduced the term *anticrack* for RLI and *quasicracks* for elastic line inclusion: they obtained similar solutions to (Atkinson, 1973) starting from the Eshelby's ellipsoidal *equivalent inclusion*, for the limit to zero of the ratio between the axes.

Despite the great amount of theoretical work produced over the years, there was no attention to investigate experimentally the stress distribution near a line stiffener, until 2008, when (Dal Corso et al., 2008; Bigoni et al., 2008), and later (Dal Corso and Bigoni, 2009), (Noselli et al., 2010) interestingly disclosed, with photo-elasticity, the *full-field* stress state of an extremely thin and stiff inclusion made of steel embedded in a transparent epoxy matrix. They validated with their experiments some intriguing aspects of the RLI problem, already known from the analytical solutions: for instance, the appearance of a *square root* singularity also for tensile loading parallel to the stiffener.

With the field of nanocomposites in rapid growth, it becomes of paramount importance to develop numerical methods that implement RLI models that could be used by materials scientists and engineers to investigate the toughness properties of both natural and man-made composites, or to imitate artificially the hierarchical structures present in nature. This topic seems to have been overlooked by researchers in numerical methods, with almost absent literature in this field. It is worth to acknowledge the significant contributions of (Radtke et al., 2010, 2011) where they employ a Partition of Unity Finite Element Method (PUFEM) to introduce short thin fibres in a cementitious matrix as a *tunnelling crack* with a finite very short thickness, not zero. The *tunnel* is introduced as a two-dimensional *Heaviside* enrichment (1 inside the fibre, 0 otherwise) over the span of the fibre. Instead, we introduce an *exactly zero* thickness. Moreover, in these works it is not reported any connections with a negative J-integral, nor comparisons with existing analytical solutions, whereas instead we make use of the relation in (Chen, 1986) and a numerically computed J-integral to validate our results in terms of Stress Intensity Factors.

Exploiting the strong relation with cracks, we used an idea recently developed (Barbieri et al., 2012; Barbieri and Petrinic, 2013b,a) for fracture in a meshfree context: the aim is to create a crack where the RLI is positioned, and then impose a rigid motion at the (anti)cracks surfaces. The orientation of the inclusion can be arbitrary inside the matrix, without restrictions imposed by the underlying discretization of the matrix.

The structure of the paper is the following: section 2 summarizes the analytical solutions available in the literature, alongside with the formulas for the extraction of the SIFs; section 3 describes the governing equations in strong and weak form and the ones arising from their discretization; section 4 presents the examples for the validation of the method, comparison with analytical solutions (full field and SIFs) and reorientation of fibres under a tensile loading; finally, conclusions 5 are drawn.

2. Analytical solutions, J-integral and Stress Intensity Factors

2.1. Analytical solution

(Atkinson, 1973) derived an analytical solution for an horizontal rigid line inclusion problem in an infinite isotropic elastic matrix under uniform remote biaxial loading σ_x^∞ and σ_y^∞. In the following, the orthogonal reference has axis x aligned with the inclusion with the origin in its middle point. The rigid line inclusion has length $2a$.

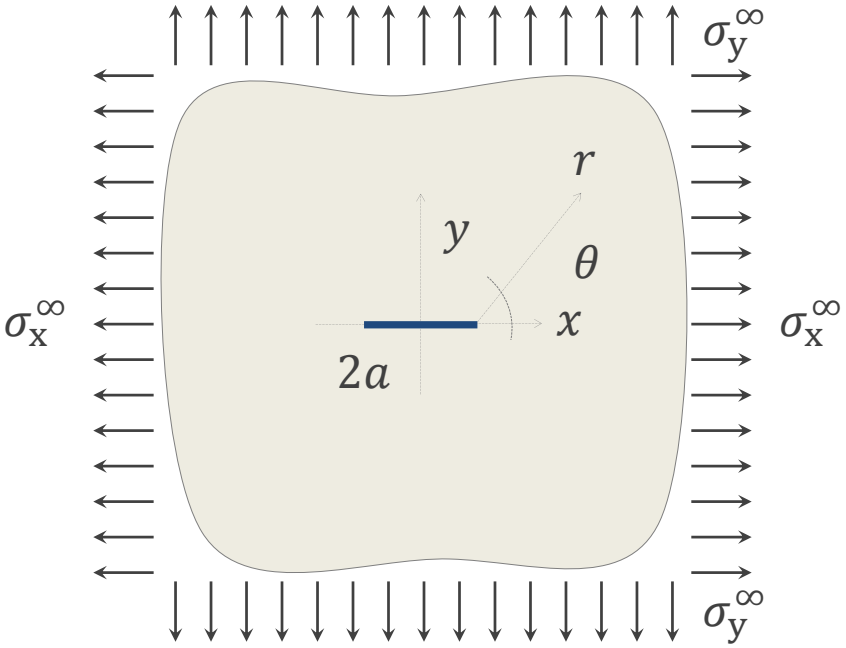

Figure 1: Reference frame and loading for the analytical solution (Atkinson, 1973)

Under uniform biaxial tension, and without the inclusion, the matrix strains uniformly, with a displacements field given by

$$u_0(x,y) = \frac{x}{8\mu}\left((\kappa+1)\sigma_x^\infty + (\kappa-3)\sigma_y^\infty\right) \tag{1}$$

$$v_0(x,y) = \frac{y}{8\mu}\left((\kappa-3)\sigma_x^\infty + (\kappa+1)\sigma_y^\infty\right) \tag{2}$$

where κ is

$$\kappa = \begin{cases} 3-4\nu & \text{plane strain} \\ \frac{3-\nu}{1+\nu} & \text{plane stress} \end{cases} \tag{3}$$

and μ is the *shear modulus* and ν is the Poisson ratio. The component ϵ_{x0} of the strain tensor given by

$$\epsilon_{x0}(x,y) = \frac{1}{8\mu}\left((\kappa+1)\sigma_x^\infty + (\kappa-3)\sigma_y^\infty\right) \tag{4}$$

The line inclusion can only move rigidly. Hence, with the rigid line inclusion now inserted in the matrix, and for the symmetry of the problem, the motion is only translational in the horizontal direction and with no rotation. For the

compatibility of the displacements, this translation must be equal to the displacement u_0 (1) at its tips ($x = \pm a,\ y = 0$). In deriving the analytical solution, (Atkinson, 1973) conveniently subtracted out the uniform strain of the matrix to obtain zero stresses at infinity. Hence,

$$\begin{cases} u(x,0) = -u_0 & |x| < a \\ v(x,0) = 0 & \forall x \end{cases} \tag{5}$$

and, for the equilibrium, $\tau_{xy} = 0 |x| > a$. Additionally, all stresses tend to zero at infinity. With these boundary conditions, the stress tensor at $y = 0$ (1) has components

$$\sigma_x = -(\kappa + 3)A\left(1 - \frac{|x|}{\sqrt{x^2 - a^2}}\right) \qquad |x| > a \tag{6}$$

$$\sigma_y = (\kappa - 1)A\left(1 - \frac{|x|}{\sqrt{x^2 - a^2}}\right) \qquad |x| > a \tag{7}$$

$$\tau_{xy} = \frac{\kappa + 1}{\sqrt{a^2 - x^2}} Ax \qquad |x| < a \tag{8}$$

where A is

$$A = \frac{1}{8}\left((\kappa + 1)\sigma_x^{\infty} + (\kappa - 3)\sigma_y^{\infty}\right) \tag{9}$$

2.2. Asymptotic near-tip solution

(Wang et al., 1985) derived a near-tip expansion of the stress fields that resembles the asymptotic crack-tip solution, namely

$$\begin{bmatrix} \sigma_x \\ \sigma_y \\ \tau_{xy} \end{bmatrix} = \frac{H_I}{\sqrt{2\pi r}} \begin{bmatrix} \cos\frac{\theta}{2}\left(\frac{\kappa+3}{2} - \sin\frac{\theta}{2}\sin\frac{3\theta}{2}\right) \\ \cos\frac{\theta}{2}\left(\frac{1-\kappa}{2} + \sin\frac{\theta}{2}\sin\frac{3\theta}{2}\right) \\ \sin\frac{\theta}{2}\left(\frac{1+\kappa}{2} + \cos\frac{\theta}{2}\cos\frac{3\theta}{2}\right) \end{bmatrix} \tag{10}$$

where r and θ is a polar coordinate system (figure 1) with $r << a$. The parameter H_I is not an equivalent Stress Intensity Factor (SIF): however, it can be related to the remote loading conditions and to the value of the J-integral, as it will be shown next.

It easy to realize that the Mode I SIF K_I is then

$$K_I = \frac{1 - \kappa}{2} H_I \tag{11}$$

Moreover, according to equation (11), K_I and H_I might be of a different sign.

2.3. Relation between SIF and analytical solution

From equation (7) and assuming $r << a$, with $r = x - a$

$$\sigma_y \approx (1 - \kappa)A\left(\frac{r + a}{\sqrt{r^2 + a^2 + 2ra - a^2}}\right) \approx (1 - \kappa)A\left(\frac{a}{\sqrt{2ra}}\right) = \frac{(1 - \kappa)A}{\sqrt{2}}\frac{\sqrt{a}}{\sqrt{r}} \tag{12}$$

Comparing with the second of (10)

$$H_I = 2A\sqrt{\pi a} \tag{13}$$

and, for (11)

$$K_I = (1-\kappa)A\sqrt{\pi a} \tag{14}$$

2.4. Relation between the SIF and the J-integral

As reported in (Chen, 1986), the J-integral for anticracks is negative. Using an integral domain method (Walters et al., 2005), the J-integral on line inclusions can be computed as follows

$$J = \int_A \boldsymbol{\sigma}\frac{\partial \mathbf{u}}{\partial x}\boldsymbol{\nabla} q \, \mathrm{d}A - \int_A W\frac{\partial q}{\partial x}\mathrm{d}A - \int_{S^+\cup S^-} \mathbf{t}^T\frac{\partial \mathbf{u}}{\partial x}\mathrm{d}S \tag{15}$$

where A is a domain enclosing the crack tip. In equation (15) an additional term appears that takes into account the presence of *non-zero* tractions $\mathbf{t}$ on the line inclusion, and $S^+ \cup S^-$ are the two sides of the anticrack. Furthermore, q is a virtual displacements scalar weight function, and W is the strain energy density. More details can be found in the appendix Appendix A.

Chen proved that

$$J = -\frac{\kappa(\kappa+1)}{8\mu}H_I^2 \tag{16}$$

Hence, the numerical SIF can be extracted from equation (16) after having computed J from equation (15)

$$H_I^{num} = \sqrt{-J\frac{8\mu}{\kappa(\kappa+1)}} \tag{17}$$

3. Governing equations

3.1. Strong form

Justified by the assumption of soft and deformable matrix, common in biological tissues, the kinematics in this paper is one of a *finite deformation*. In addition, finite deformation of the matrix allows to demonstrate the effectiveness of the numerical method for large rotations of the RLI. The continuum formulation is *Total Lagrangian* (TL), with Ω_0 being the *reference configuration*, and Ω the *deformed configuration*. In the following, $\mathbf{X}$ denote the *material coordinates* and $\mathbf{x}$ the deformation. We will also consider *static* problems, and for ease of readability, this section treats only one anticrack. However, the equations extend easily to multiple anticracks, as showed in section 3.5.

In a discrete meshfree setting, the *anticracks* can be explicitly introduced by the *intrinsic enrichment* presented in (Barbieri et al., 2012; Barbieri and Petrinic, 2013b,a), which is based only on geometry (*distance fields*) therefore completely independent from the particular constitutive model.

The Boundary Value Problem (BVP) is the following: find the displacement fields $\mathbf{u} : \Omega_0 \subset \mathbb{R}^3 \rightarrow \mathbb{R}^3$ such that it satisfies the following equilibrium equations in a Lagrangian description, in absence of body forces:

$$\begin{cases} \nabla_0 \cdot \mathbf{P} = 0 & \mathbf{X} \in \Omega_0 \\ \mathbf{n}_0 \cdot \mathbf{P} = \mathbf{t}_0 & \mathbf{X} \in \Gamma_t^0 \\ \mathbf{u} = \bar{\mathbf{u}} & \mathbf{X} \in \Gamma_u^0 \end{cases} \tag{18}$$

where $\mathbf{P}$ is the *First Piola-Kirchhoff* stress, $\mathbf{n}_0$ is the normal unity vector (in the reference configuration) of the boundary Γ_t^0 where the traction $\mathbf{t}_0$ is prescribed, and Γ_u^0 is the boundary where the displacement $\bar{\mathbf{u}}$ is prescribed. The symbol ∇_0 denotes the gradient with respect to the material coordinates.

In addition, a rigid motion must be imposed on the surfaces of the inclusion: calling S^+ the top side of the inclusion and S^- the bottom side

$$\begin{cases} \mathbf{u}^+ - \mathbf{u}_L = 0 & \mathbf{X} \in S^+ \\ \mathbf{u}^- - \mathbf{u}_L = 0 & \mathbf{X} \in S^- \end{cases} \tag{19}$$

where $\mathbf{u}_L$ is the rigid motion of the inclusion, which can be decomposed in a rotation and a translation. In a TL framework, the undeformed configuration $\mathbf{X}_L$ can me mapped into the current configuration of the inclusion $\mathbf{x}_L$

$$\mathbf{x}_L = \mathbf{c} + \mathbf{R}\,\mathbf{X}_L \tag{20}$$

where $\mathbf{c}$ is the deformation of the center of rotation (which may not belong to the RLI), $\mathbf{R}$ is a rotation matrix (in 2D)

$$\mathbf{R} = \begin{bmatrix} \cos\theta & -\sin\theta \\ \sin\theta & \cos\theta \end{bmatrix} \tag{21}$$

Thus, the displacement $\mathbf{u}_L$ of the inclusion in equation (19) is given by

$$\mathbf{u}_L = \mathbf{x}_L - \mathbf{X}_L = \mathbf{c} + (\mathbf{R} - \mathbf{I})\,\mathbf{X}_L \tag{22}$$

or, in an expanded form

$$\begin{cases} u_L = c_x + (\cos\theta - 1)\ X_L - \sin\theta\ Y_L \\ v_L = c_y + \sin\theta\ X_L + (\cos\theta - 1)\ Y_L \end{cases} \tag{23}$$

From equations (23) emerges that there are 3 additional unknowns (c_x, c_y, θ) for each rigid inclusion. Such motion is not imposed a priori, but is a a consequence of the equilibrium.

3.2. Weak form

Using the displacement $\mathbf{u}$ as a test function for equations (18), the variational form can be written as

$$\int_{\Omega_0} \delta\mathbf{E} : \mathbf{S}\mathrm{d}\Omega_0 - \int_{\Gamma_t^0} \delta\mathbf{u}^T\mathbf{t}_0\ \mathrm{d}\Gamma_t^0 + \alpha \int_{\Gamma_u^0} \delta\,(\mathbf{u} - \bar{\mathbf{u}})^T\,(\mathbf{u} - \bar{\mathbf{u}})\ \mathrm{d}\Gamma_u^0 +$$

$$+\alpha \int_{S^+} \delta\,(\mathbf{u}^+ - \mathbf{u}_L)^T\,(\mathbf{u}^+ - \mathbf{u}_L)\,\mathrm{d}S^+ + \alpha \int_{S^-} \delta\,(\mathbf{u}^- - \mathbf{u}_L)^T\,(\mathbf{u}^- - \mathbf{u}_L)\,\mathrm{d}S^- = 0 \tag{24}$$

where $\mathbf{E}$ is the Green-Lagrange strain, $\mathbf{S}$ is the Second Piola-Kirchhoff stress, α is a penalty parameter (usually a large number of the same order of magnitude of the elastic properties) used to enforce the essential boundary conditions. The Green Lagrange strain is defined as

$$\mathbf{E} = \frac{1}{2}\left(\mathbf{F}^T\mathbf{F} - \mathbf{I}\right) \tag{25}$$

with $\mathbf{F}$ being the deformation gradient. The Second Piola-Kirchhoff stress is related to $\mathbf{P}$ and to the Cauchy stress $\boldsymbol{\sigma}$ with the following relations:

$$\mathbf{S} = \mathbf{F}^{-1}\,\mathbf{P} \qquad \boldsymbol{\sigma} = \frac{1}{J}\,\mathbf{F}\,\mathbf{S}\,\mathbf{F}^T \tag{26}$$

with J being the Jacobian of the deformation gradient. The variations in (24) can be expanded as follows:

$$\delta\left(\mathbf{u}^+ - \mathbf{u}_L\right)^T = \delta\mathbf{u}^{+T} - \delta\mathbf{u}_L^T \tag{27}$$

where

$$\delta\mathbf{u}^{+T} = \delta\mathbf{d}^T\begin{bmatrix}\boldsymbol{\phi}_+ & 0\\ 0 & \boldsymbol{\phi}_+\end{bmatrix} \tag{28}$$

where $\boldsymbol{\phi}_+$ are the shape functions of the discretization nodes on $S^+$and $\mathbf{d}$ the global vector of the nodal unknowns. From equation (23)

$$\delta\mathbf{u}_L^T = \delta\mathbf{c}^T + \delta\theta\begin{bmatrix}-\sin\theta\,X_L - \cos\theta\,Y_L & \cos\theta\,X_L - \sin\theta\,Y_L\end{bmatrix} \tag{29}$$

Therefore, the penalty term of the rigid line inclusion in equation (24) for S^+ can be written as

$$\alpha\delta\mathbf{d}^T\int_{S^+}\begin{bmatrix}\boldsymbol{\phi}_+\,(u^+ - u_L)\\ \boldsymbol{\phi}_+\,(v^+ - v_L)\end{bmatrix}\mathrm{d}S^+ + \alpha\delta\mathbf{c}^T\int_{S^+}\begin{bmatrix}(u_L - u^+)\\ (v_L - v^+)\end{bmatrix}\mathrm{d}S^+ +$$

$$\alpha\delta\theta\int_{\Gamma_c}(\sin\theta\,X_L + \cos\theta\,Y_L)\,(u^+ - u_L) + (-\cos\theta\,X_L + \sin\theta\,Y_L)\,(v^+ - v_L)\,\mathrm{d}S^+ \tag{30}$$

and similarly for S^-.

3.3. Discretized equations of motion

The approximation $\mathbf{u}^h$ of the field variable $\mathbf{u}(\mathbf{X})$ in equation (18) is an expansion

$$\mathbf{u}^h(\mathbf{X}) = \sum_I^N \phi_I(\mathbf{X})\mathbf{d}_I \tag{31}$$

where N is the number of discretization points, $\phi_I : \Omega \to \mathbb{R}$ is the $I-$th shape function and $\mathbf{U}_I$ is the nodal value related to the position $\mathbf{X}_I$. The expressions for the shape functions in equation (31) depend on the method employed for the discretization: in this paper we use the Reproducing Kernel Particle Method (RKPM) (Liu et al., 1995) because it allows a fast introduction of crack surfaces without *remeshing* (Barbieri and Meo, 2012; Barbieri et al., 2012; Barbieri and Petrinic, 2013a,b). On these crack surfaces, a rigid motion (22) is enforced.

Following Belytschko et al. (2000), using equation (31), the discretized variation of the deformation gradient becomes

$$\delta\mathbf{F}^h = \delta\mathbf{d}\,\mathcal{B}_0^T \tag{32}$$

with

$$\mathcal{B}_0^T = \begin{bmatrix} \dfrac{\partial\boldsymbol{\phi}^T}{\partial X} & \dfrac{\partial\boldsymbol{\phi}^T}{\partial Y} & \dfrac{\partial\boldsymbol{\phi}^T}{\partial Z} \end{bmatrix} \tag{33}$$

and the following holds

$$\delta\mathbf{F} : \mathbf{P} = \delta\mathbf{E} : \mathbf{S} \tag{34}$$

Replacing (31) into (18) and considering equation (30), the following equilibrium equations are obtained

$$\begin{cases} \mathbf{F}^{(i)}(\mathbf{d}) - \mathbf{F}^{(e)} + \mathbf{F}_d^+(\mathbf{d},\mathbf{c},\theta) + \mathbf{F}_d^-(\mathbf{d},\mathbf{c},\theta) = 0 \\ \mathbf{F}_c^+(\mathbf{d},\mathbf{c},\theta) + \mathbf{F}_c^-(\mathbf{d},\mathbf{c},\theta) = 0 \\ F_\theta^+(\mathbf{d},\mathbf{c},\theta) + F_\theta^-(\mathbf{d},\mathbf{c},\theta) \end{cases} \tag{35}$$

where $\mathbf{F}^{(e)}$ is the *external forces* vector

$$\mathbf{F}_I^e = \int_{\Gamma_u} \phi_I^T \mathbf{t}_0 \mathrm{d}\Gamma_u \tag{36}$$

$\mathbf{F}_d^+$ (and similarly $\mathbf{F}_d^-$) is the coupling between the matrix and the inclusion

$$\mathbf{F}_d^+(\mathbf{d},\mathbf{c},\theta) = \alpha \int_{S^+} \begin{bmatrix} \boldsymbol{\phi}_+ (u^+ - u_L) \\ \boldsymbol{\phi}_+ (v^+ - v_L) \end{bmatrix} \mathrm{d}S^+ \tag{37}$$

$\mathbf{F}_c^+$ (and similarly $\mathbf{F}_c^-$)

$$\mathbf{F}_c^+(\mathbf{d},\mathbf{c},\theta) = \alpha \int_{S^+} \begin{bmatrix} (u_L - u^+) \\ (v_L - v^+) \end{bmatrix} \mathrm{d}S^+ \tag{38}$$

F_θ^+ (and similarly F_θ^-)

$$F_\theta^+(\mathbf{d},\mathbf{c},\theta) = \int_{S^+} (\sin\theta X_L + \cos\theta Y_L)(u^+ - u_L) + (-\cos\theta X_L + \sin\theta Y_L)(v^+ - v_L)\,\mathrm{d}S^+ \tag{39}$$

and finally, $\mathbf{F}^{(i)}$ is the *internal forces* vector that depends on the *constitutive model* of the material

$$\delta\mathbf{d}^T\mathbf{F}^{(i)}(\mathbf{d}) = \int_{\Omega_0} \delta\mathbf{E}^h : \mathbf{S}^h \,\mathrm{d}\Omega_0 = \int_{\Omega_0} \delta\mathbf{F}^h : \mathbf{P}^h \,\mathrm{d}\Omega_0 = \delta\mathbf{d}^T \int_{\Omega_0} \begin{bmatrix} \dfrac{\partial\boldsymbol{\phi}}{\partial X} P_{11}(\mathbf{d}) + \dfrac{\partial\boldsymbol{\phi}}{\partial Y} P_{21}(\mathbf{d}) \\ \dfrac{\partial\boldsymbol{\phi}}{\partial X} P_{12}(\mathbf{d}) + \dfrac{\partial\boldsymbol{\phi}}{\partial Y} P_{22}(\mathbf{d}) \end{bmatrix} \mathrm{d}\Omega_0 \tag{40}$$

3.4. Tangent stiffness matrix

Equation (35) is nonlinear in $(\mathbf{d},\mathbf{c},\theta)$. For n inclusions, the total number of unknowns is then $2N + 3n$ in two dimensions. Therefore, solving (35) requires an iterative numerical scheme (for instance *Newton - Raphson*). For

each iteration, it is necessary to compute the the *tangent stiffness matrix* (or the *Jaobian*) K_T that is the gradient of the left-hand side of equation (35) with respect to the unknowns $(\mathbf{d}, \mathbf{c}, \theta)$. This gradient has the following form:

$$\mathbf{K}_T = \begin{bmatrix} \dfrac{\partial \mathbf{F}^{(i)}}{\partial \mathbf{d}} + \dfrac{\partial \mathbf{F}_d^+}{\partial \mathbf{d}} + \dfrac{\partial \mathbf{F}_d^-}{\partial \mathbf{d}} & \dfrac{\partial \mathbf{F}_d^+}{\partial \mathbf{c}} + \dfrac{\partial \mathbf{F}_d^-}{\partial \mathbf{c}} & \dfrac{\partial \mathbf{F}_d^+}{\partial \theta} + \dfrac{\partial \mathbf{F}_d^-}{\partial \theta} \\ \dfrac{\partial \mathbf{F}_c^+}{\partial \mathbf{d}} + \dfrac{\partial \mathbf{F}_c^-}{\partial \mathbf{d}} & \dfrac{\partial \mathbf{F}_c^+}{\partial \mathbf{c}} + \dfrac{\partial \mathbf{F}_c^-}{\partial \mathbf{c}} & \dfrac{\partial \mathbf{F}_c^+}{\partial \theta} + \dfrac{\partial \mathbf{F}_c^-}{\partial \theta} \\ \dfrac{\partial F_\theta^+}{\partial \mathbf{d}} + \dfrac{\partial F_\theta^-}{\partial \mathbf{d}} & \dfrac{\partial F_\theta^+}{\partial \mathbf{c}} + \dfrac{\partial F_\theta^-}{\partial \mathbf{c}} & \dfrac{\partial F_\theta^+}{\partial \theta} + \dfrac{\partial F_\theta^-}{\partial \theta} \end{bmatrix} \tag{41}$$

We will show in the following that the matrix in (41) is symmetric. Indeed, the entries are

$$\frac{\partial \mathbf{F}_d^+}{\partial \mathbf{d}} = \int_{S^+} \begin{bmatrix} \boldsymbol{\phi}_+ \boldsymbol{\phi}_+^T & 0 \\ 0 & \boldsymbol{\phi}_+ \boldsymbol{\phi}_+^T \end{bmatrix} \mathrm{d}S^+ \tag{42}$$

$$\frac{\partial \mathbf{F}_d^+}{\partial \mathbf{c}} = \int_{S^+} \begin{bmatrix} -\boldsymbol{\phi}_+ & 0 \\ 0 & -\boldsymbol{\phi}_+ \end{bmatrix} \mathrm{d}S^+ = \frac{\partial \mathbf{F}_c^{+\,T}}{\partial \mathbf{d}} \tag{43}$$

$$\frac{\partial \mathbf{F}_d^+}{\partial \theta} = \int_{S^+} \begin{bmatrix} \boldsymbol{\phi}_+ \left(\sin\theta X_L + \cos\theta Y_L\right) \\ \boldsymbol{\phi}_+ \left(-\cos\theta X_L + \sin\theta Y_L\right) \end{bmatrix} \mathrm{d}S^+ = \frac{\partial F_\theta^{+\,T}}{\partial \mathbf{d}} \tag{44}$$

$$\frac{\partial \mathbf{F}_c^+}{\partial \mathbf{c}} = \int_{S^+} \mathrm{d}S^+ \mathbf{I} \tag{45}$$

where $\mathbf{I}$ is the *identity* matrix,

$$\frac{\partial \mathbf{F}_c^+}{\partial \theta} = \int_{S^+} \begin{bmatrix} -\left(\sin\theta X_L + \cos\theta Y_L\right) \\ -\left(-\cos\theta X_L + \sin\theta Y_L\right) \end{bmatrix} \mathrm{d}S^+ = \frac{\partial F_\theta^{+\,T}}{\partial \mathbf{c}} \tag{46}$$

$$\frac{\partial F_\theta^+}{\partial \theta} = \int_{S^+} \left(\sin\theta X_L + \cos\theta Y_L\right)^2 + \left(\cos\theta X_L - \sin\theta Y_L\right)^2 \mathrm{d}S^+ \tag{47}$$

It can be shown that

$$\frac{\partial \mathbf{F}^{(i)}}{\partial \mathbf{d}} = \left(\frac{\partial \mathbf{F}^{(i)}}{\partial \mathbf{d}}\right)_g + \left(\frac{\partial \mathbf{F}^{(i)}}{\partial \mathbf{d}}\right)_m \tag{48}$$

where subscript $(\cdot)_g$ stands for *geometric part*, which takes into account geometrical nonlinearities

$$\left(\frac{\partial \mathbf{F}^{(i)}}{\partial \mathbf{d}}\right)_g = \int_{\Omega_0} \begin{bmatrix} \mathcal{B}_0^T \mathbf{S}(\mathbf{d}) \mathcal{B}_0 & \\ & \mathcal{B}_0^T \mathbf{S}(\mathbf{d}) \mathcal{B}_0 \end{bmatrix} \mathrm{d}\Omega_0 \tag{49}$$

whilst $(\cdot)_m$ stands for the *material part*, which takes into account material nonlinearities

$$\left(\frac{\partial \mathbf{F}^{(i)}}{\partial \mathbf{d}}\right)_m = \int_{\Omega_0} \mathbf{B}^T(\mathbf{d})\, \mathbf{C}^{SE}(\mathbf{d})\, \mathbf{B}(\mathbf{d})\, \mathrm{d}\Omega_0 \tag{50}$$

where

$$\mathbf{B}(\mathbf{d}) = \begin{bmatrix} F_{11}\dfrac{\partial \boldsymbol{\phi}}{\partial X}^T & F_{21}\dfrac{\partial \boldsymbol{\phi}}{\partial X}^T \\ F_{12}\dfrac{\partial \boldsymbol{\phi}}{\partial Y}^T & F_{22}\dfrac{\partial \boldsymbol{\phi}}{\partial Y}^T \\ F_{11}\dfrac{\partial \boldsymbol{\phi}}{\partial Y}^T + F_{12}\dfrac{\partial \boldsymbol{\phi}}{\partial X}^T & F_{21}\dfrac{\partial \boldsymbol{\phi}}{\partial Y}^T + F_{22}\dfrac{\partial \boldsymbol{\phi}}{\partial X}^T \end{bmatrix} \tag{51}$$

and $\mathbf{C}^{SE}$ is the *Second Elasticity Tensor* in Voigt form, defined, in tensorial form, as

$$\mathbb{C}^{SE} = \frac{\partial \mathbf{S}}{\partial \mathbf{E}} \tag{52}$$

3.5. *Multiple rigid line inclusions*

For multiple anticracks, equation (24) modifies as

$$\int_{\Omega_0} \delta\mathbf{E} : \mathbf{S} \mathrm{d}\Omega_0 - \int_{\Gamma_t^0} \delta\mathbf{u}^T \mathbf{t}_0 \, \mathrm{d}\Gamma_t^0 + \alpha \int_{\Gamma_u^0} \delta(\mathbf{u} - \bar{\mathbf{u}})^T (\mathbf{u} - \bar{\mathbf{u}}) \, \mathrm{d}\Gamma_u^0 +$$

$$+ \sum_{i=1}^{n_a} \alpha \int_{S_i^+} \delta(\mathbf{u}^+ - \mathbf{u}_{L,i})^T (\mathbf{u}^+ - \mathbf{u}_{L,i}) \, \mathrm{d}S_i^+ + \alpha \int_{S_i^-} \delta(\mathbf{u}^- - \mathbf{u}_{L,i})^T (\mathbf{u}^- - \mathbf{u}_{L,i}) \, \mathrm{d}S_i^- = 0 \tag{53}$$

with n_a being the number of anticracks. With similar steps as in section 3.1 and 3.2, the discretized equations of motion are

$$\begin{cases} \mathbf{F}^{(i)}(\mathbf{d}) - \mathbf{F}^{(e)} + \sum_{i=1}^{n_a} \mathbf{F}_d^+(\mathbf{d}, \mathbf{c}_i, \theta_i) + \mathbf{F}_d^-(\mathbf{d}, \mathbf{c}_i, \theta_i) = 0 \\ \mathbf{F}_{c_1}^+(\mathbf{d}, \mathbf{c}_1, \theta_1) + \mathbf{F}_{c_1}^-(\mathbf{d}, \mathbf{c}_1, \theta_1) = 0 \\ \mathbf{F}_{c_2}^+(\mathbf{d}, \mathbf{c}_2, \theta_2) + \mathbf{F}_{c_2}^-(\mathbf{d}, \mathbf{c}_2, \theta_2) = 0 \\ \dots \\ \mathbf{F}_{c_{n_a}}^+(\mathbf{d}, \mathbf{c}_{n_a}, \theta_{n_a}) + \mathbf{F}_{c_{n_a}}^-(\mathbf{d}, \mathbf{c}_{n_a}, \theta_{n_a}) = 0 \\ F_{\theta_1}^+(\mathbf{d}, \mathbf{c}_1, \theta_1) + F_{\theta_1}^-(\mathbf{d}, \mathbf{c}_1, \theta_1) = 0 \\ F_{\theta_2}^+(\mathbf{d}, \mathbf{c}_2, \theta_2) + F_{\theta_2}^-(\mathbf{d}, \mathbf{c}_2, \theta_2) = 0 \\ \dots \\ F_{\theta_{n_a}}^+(\mathbf{d}, \mathbf{c}_{n_a}, \theta_{n_a}) + F_{\theta_{n_a}}^-(\mathbf{d}, \mathbf{c}_{n_a}, \theta_{n_a}) = 0 \end{cases} \tag{54}$$

where the terms are analogous to equations (37), (38) and (39). Similarly, the tangent stiffness matrix is given by:

$$\mathbf{K}_T = \begin{bmatrix} \dfrac{\partial \mathbf{F}^{(i)}}{\partial \mathbf{d}} + \sum_{i=1}^{n_a} \dfrac{\partial \mathbf{F}_d^+}{\partial \mathbf{d}} + \dfrac{\partial \mathbf{F}_d^-}{\partial \mathbf{d}} & \mathbf{K}_{dc}^T & \mathbf{K}_{d\theta}^T \\ \mathbf{K}_{dc} & \mathbf{K}_{cc} & \mathbf{K}_{c\theta}^T \\ \mathbf{K}_{d\theta} & \mathbf{K}_{c\theta} & \mathbf{K}_{\theta\theta} \end{bmatrix} \tag{55}$$

where

$$\mathbf{K}_{dc}^{T} = \left[\frac{\partial \mathbf{F}_d^+}{\partial \mathbf{c}_1} + \frac{\partial \mathbf{F}_d^-}{\partial \mathbf{c}_1} \quad \frac{\partial \mathbf{F}_d^+}{\partial \mathbf{c}_2} + \frac{\partial \mathbf{F}_d^-}{\partial \mathbf{c}_2} \quad \cdots \quad \frac{\partial \mathbf{F}_d^+}{\partial \mathbf{c}_{n_a}} + \frac{\partial \mathbf{F}_d^-}{\partial \mathbf{c}_{n_a}} \right] \tag{56}$$

$$\mathbf{K}_{d\theta}^{T} = \left[\frac{\partial \mathbf{F}_d^+}{\partial \theta_1} + \frac{\partial \mathbf{F}_d^-}{\partial \theta_1} \quad \frac{\partial \mathbf{F}_d^+}{\partial \theta_2} + \frac{\partial \mathbf{F}_d^-}{\partial \theta_2} \quad \cdots \quad \frac{\partial \mathbf{F}_d^+}{\partial \theta_{n_a}} + \frac{\partial \mathbf{F}_d^-}{\partial \theta_{n_a}} \right] \tag{57}$$

$$\mathbf{K}_{c\theta} = \begin{bmatrix} \frac{\partial \mathbf{F}_{c_1}^+}{\partial \theta_1} + \frac{\partial \mathbf{F}_{c_1}^-}{\partial \theta_1} & & & \cdots & \\ & \frac{\partial \mathbf{F}_{c_2}^+}{\partial \theta_2} + \frac{\partial \mathbf{F}_{c_2}^-}{\partial \theta_2} & \cdots & & \\ & & \ddots & & \\ & & \cdots & \frac{\partial \mathbf{F}_{c_{n_a}}^+}{\partial \theta_{n_a}} + \frac{\partial \mathbf{F}_{c_{n_a}}^-}{\partial \theta_{n_a}} \end{bmatrix} \tag{58}$$

$$\mathbf{K}_{cc} = \begin{bmatrix} \frac{\partial \mathbf{F}_{c_1}^+}{\partial \mathbf{c}_1} + \frac{\partial \mathbf{F}_{c_1}^-}{\partial \mathbf{c}_1} & & & \cdots & \\ & \frac{\partial \mathbf{F}_{c_2}^+}{\partial \mathbf{c}_2} + \frac{\partial \mathbf{F}_{c_2}^-}{\partial \mathbf{c}_2} & \cdots & & \\ & & \ddots & & \\ & & \cdots & \frac{\partial \mathbf{F}_{c_{n_a}}^+}{\partial \mathbf{c}_{n_a}} + \frac{\partial \mathbf{F}_{c_{n_a}}^-}{\partial \mathbf{c}_{n_a}} \end{bmatrix} \tag{59}$$

$$\mathbf{K}_{\theta\theta} = \begin{bmatrix} \frac{\partial F_{\theta_1}^+}{\partial \theta_1} + \frac{\partial F_{\theta_1}^-}{\partial \theta_1} & & & \cdots & \\ & \frac{\partial F_{\theta 2}^+}{\partial \theta_2} + \frac{\partial F_{\theta_2}^-}{\partial \theta_2} & \cdots & & \\ & & \ddots & & \\ & & \cdots & \frac{\partial F_{\theta n_a}^+}{\partial \theta_{n_a}} + \frac{\partial F_{\theta_{n_a}}^-}{\partial \theta_{n_a}} \end{bmatrix} \tag{60}$$

where the entries in these matrices are analogous to equations (42), (43), (44), (45), (46) and (47).

4. Numerical examples

4.1. Comparisons of SIFs with analytical solutions

For ease of comparison with the analytical solutions (6), (7), (8) and (10), the finite deformation in this section is linearized to reconcile with the analytical results in section 2. The matrix is then an isotropic linear elastic body, defined by shear modulus μ and Poisson ratio ν, both in plane stress and plane strain. Nonetheless the approach is

general, and applicable to non-linear constitutive models, as in section 4.7. The nodal spacing (or *mesh size*) will be indicated in the following with h. The radius for the numerical computation of the *J-integral* (see appendix Appendix A) in all cases was varied from 0.4 a to 0.7 a to verify the path independence of the *J-integral*. The values are 0.5 a are reported in the following tables.

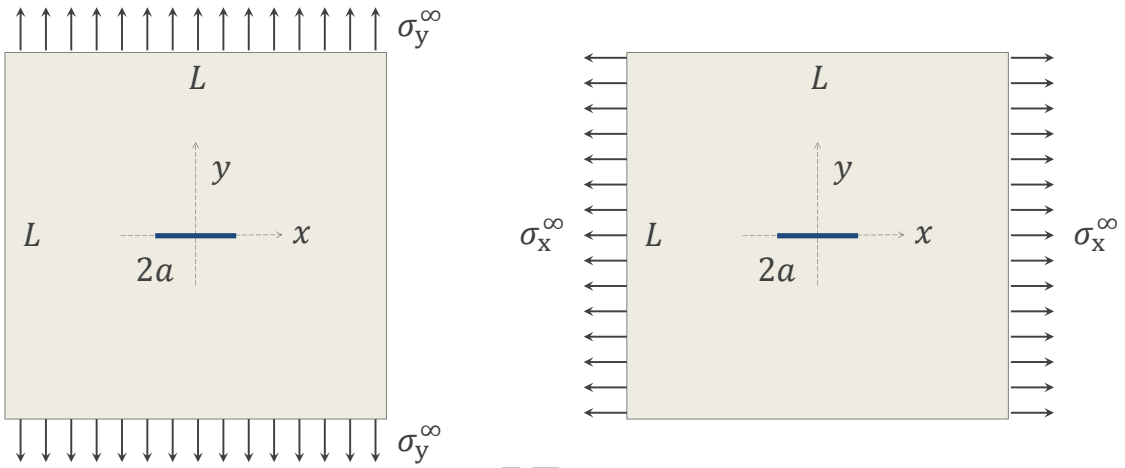

(a) Vertical loading

(b) Horizontal loading

Figure 2: Mode I anticrack. Thin black line: rigid line inclusion

4.2. Mode I under vertical tensile loading

In this section we will consider a central horizontal line inclusion embedded in a rectangular matrix subjected to a vertical tensile loading (figure 2a). Figure 3 shows the distribution of the stress tensor and the *Von Mises* stress inside the matrix: the stress concentrations at the tips of a relatively short inclusion (0.15 L) are clearly visible. These concentrations are singular for $r = 0$, as in equations (8), (6) and (7). *The functional space of the approximation* (31) *does not contain singular functions, the singularity cannot appear in the computed stresses: however, as visible in figures 4, the numerical solution can capture with great accuracy the analytical solution near the tips.* **Most importantly, the method does capture stress intensities**. Indeed, a significant comparison is reported in tables 1, 2 and 3 where the numerical values of the J-integrals (equations (16) and (17)) for different *mesh sizes* are compared to the value H_I (equation (13)), which is connected to the theoretical Stress Intensity Factor K_I (equation (14)). Tables 1, 2 and 3 show rapid convergence to the analytical value of H_I, for a relatively short inclusions (close to the hypothesis of infinite matrix, see section 2.1). Table 3 shows that even with a small number of nodes per half-length (5) it is possible to obtain the analytical answer with a small error (around 5%). It is interesting to notice that for the cases in tables 2 and 3 the values of H_I are negative. However, this does not mean a reversed stress singularity: using $\nu = 0.3$ and Young modulus $E = 50$ GPa, and applying equation (11), it is obtained a $K_I = 0.0324$ Pa $\sqrt{\text{m}}$ for $a = 0.075$ L and

$K_I = 0.0264$ Pa $\sqrt{\text{m}}$ for $a = 0.05\ L$. The sign of K_I determines the sign of the singularity (see equation (10)), and it is found consistently to be positive.

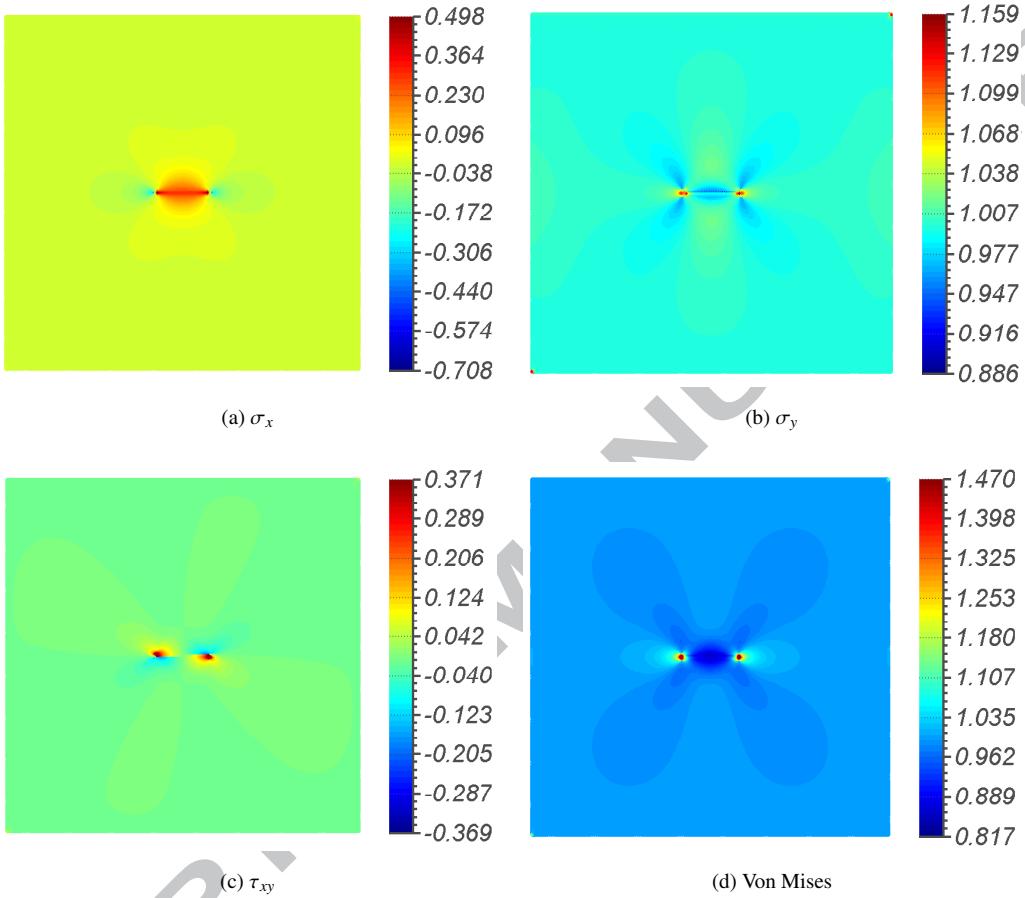

(a) σ_x (b) σ_y

(c) τ_{xy} (d) Von Mises

Figure 3: Mode I under vertical loading: stress tensor normalized to σ_y^∞, $L = 1$ m and $a = 0.075L$

4.3. Mode I under vertical compressive loading

Nonetheless, conversely to cracks, rigid line inclusion can have negative Mode I stress intensity factors, because the rigid motion of the inclusion always prevents a negative displacement jump. This case is the one in section 4.2 ($a = 0.05\ L$) with a reversed load, for which the computed stress intensity factor is $K_I = -0.0264$ Pa $\sqrt{\text{m}}$. In this test, 5 nodes per half length were employed.

4.4. Mode I under horizontal tensile loading

Another difference from cracks, is the presence of a stress singularity for loading parallel to the inclusion. The value of K_I needs to be computed with a different formula than (14): indeed, applying (14) with $a = 0.075\ L$, $\nu = 0.3$, $E = 50$ GPa and $\sigma_x^\infty > 0$, $\sigma_y^\infty = 0$ leads to $H_I = 0.1888$ Pa $\sqrt{\text{m}}$ and $K_I = -0.0755$Pa $\sqrt{\text{m}}$, which is negative and

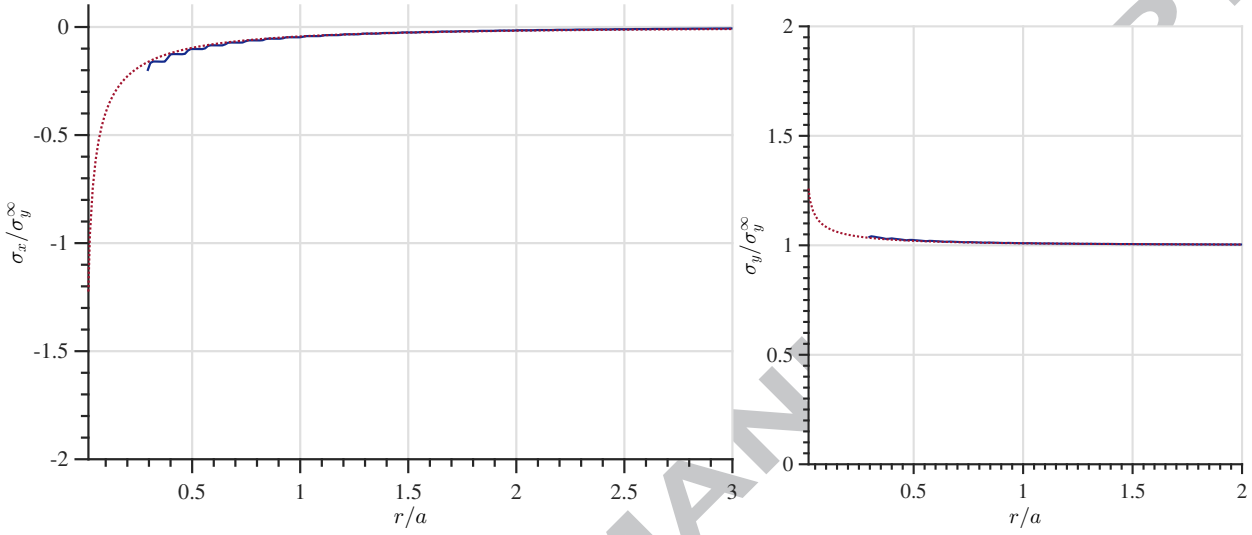

(a) σ_x

(b) σ_y

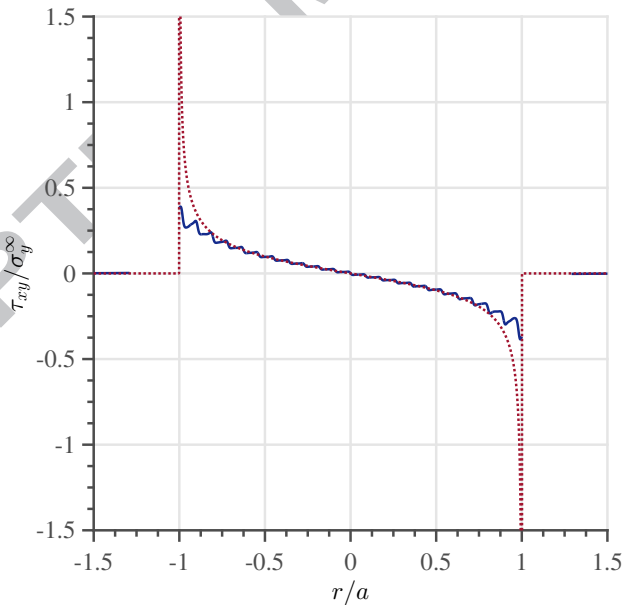

(c) τ_{xy}

Figure 4: Numerical (continuous line) and analytical (dashed line) solutions (Atkinson, 1973) according to equations (6), (7) and (8) for the vertical tensile loading (figure 2a)

h/a	a/h	H_I numerical [Pa $\sqrt{\text{m}}$]	Error %
0.100	10	0.0960	2.78
0.067	15	0.0950	1.71
0.050	20	0.0945	1.18

Table 1: Convergence analysis for the test in figure 2a in plane strain with $a = 0.01$ L: $H_I = 0.0934$ Pa $\sqrt{\text{m}}$

h/a	a/h	H_I numerical [Pa $\sqrt{\text{m}}$]	Error %
0.133	7.50	0.0856	5.81
0.089	11.25	0.0846	4.57
0.067	15.00	0.0840	3.83

Table 2: Convergence analysis for the test in figure 2a in plane strain with $a = 0.075$ L: $H_I = -0.0809$ Pa $\sqrt{\text{m}}$

h/a	a/h	H_I numerical [Pa $\sqrt{\text{m}}$]	Error %
0.200	5.00	0.0696	5.30
0.133	7.50	0.0678	2.57
0.100	10.0	0.0658	0.46

Table 3: Convergence analysis for the test in figure 2a in plane strain with $a = 5\%$ L: $H_I = -0.0661$ Pa $\sqrt{\text{m}}$

counter-intuitive. In fact, figure 5a shows a positive singularity in the σ_x plot. The negative value so calculated corresponds to the σ_y distribution (figure 5b). To get a consistent K_I for figure 5a, let us consider equation (10): the expression for σ_x for $\theta = 0$ is

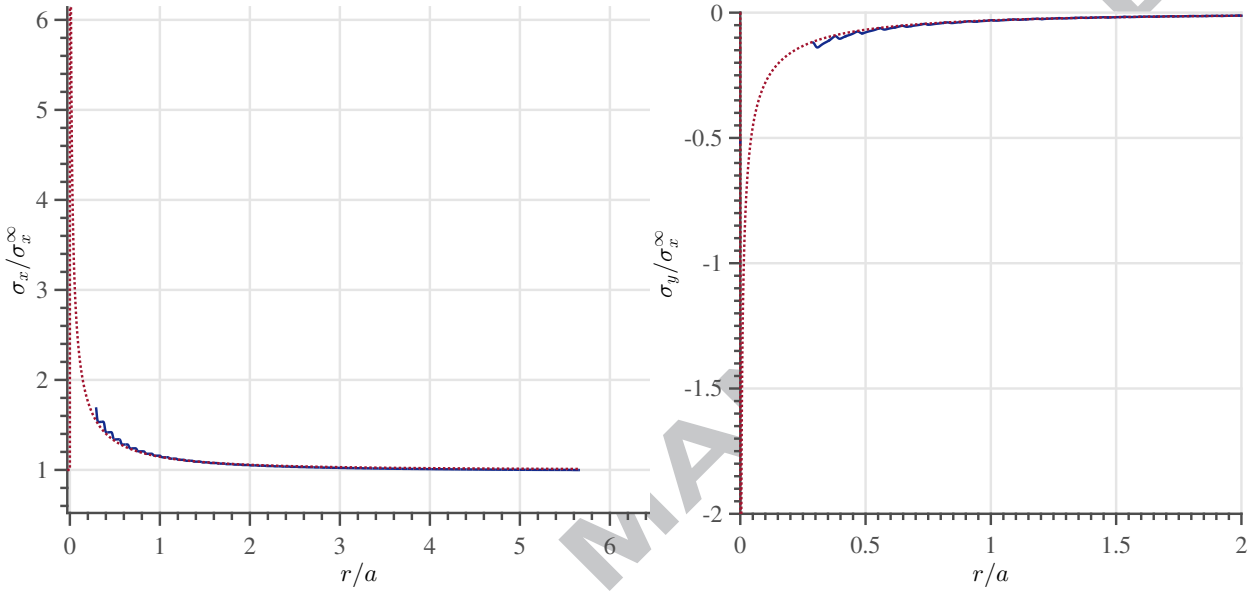

(a) σ_x (b) σ_y

Figure 5: Numerical (continuous line) and analytical (dashed line) solutions (Atkinson, 1973) according to equations (6), (7) for the horizontal tensile loading (figure 2b)

$$\sigma_y(r, \theta = 0) = \frac{H_I}{\sqrt{2\pi r}} \left(\frac{\kappa + 3}{2} \right) \tag{61}$$

hence, the correct expression for K_I under loading parallel to the anticrack is

$$K_I = (\kappa + 3)\, A \sqrt{\pi a} \tag{62}$$

Substituting the values in equation (62) leads to $K_I = 0.4530$ Pa $\sqrt{\text{m}}$, which is correctly positive. Comparing the H_I values for different loading conditions is therefore more convenient than comparing K_I, because the expression for H_I is independent from the relative position between loading and inclusion.

Tables 4, 5 and 6 show that good convergence is obtained also for the inclusion under parallel loading.

4.5. Mode I under horizontal compressive loading

Analogously to the vertical compressive loading in section 4.3, there is a singularity in the stress also for horizontal compressive loading, as showed in figure 6, captured quite accurately by the proposed numerical scheme.

h/a	a/h	H_I numerical [Pa $\sqrt{\text{m}}$]	Error %
0.100	10	0.2221	1.88
0.067	15	0.2215	1.61
0.050	20	0.2200	0.92

Table 4: Convergence analysis for the test in figure 2b in plane strain with $a = 0.10$ L: $H_I = 0.2180$ Pa $\sqrt{\text{m}}$

h/a	a/h	H_I numerical [Pa $\sqrt{\text{m}}$]	Error %
0.133	7.50	0.1974	4.56
0.089	11.25	0.1958	3.71
0.067	15.00	0.1947	3.13

Table 5: Convergence analysis for the test in figure 2b in plane strain with $a = 0.075$ L: $H_I = 0.1888$ Pa $\sqrt{\text{m}}$

h/a	a/h	H_I numerical [Pa $\sqrt{\text{m}}$]	Error %
0.200	5.00	0.1618	5.00
0.133	7.50	0.1583	2.73
0.100	10.0	0.1577	2.34

Table 6: Convergence analysis for the test in figure 2b in plane strain with $a = 0.05$ L: $H_I = 0.1577$ Pa $\sqrt{\text{m}}$

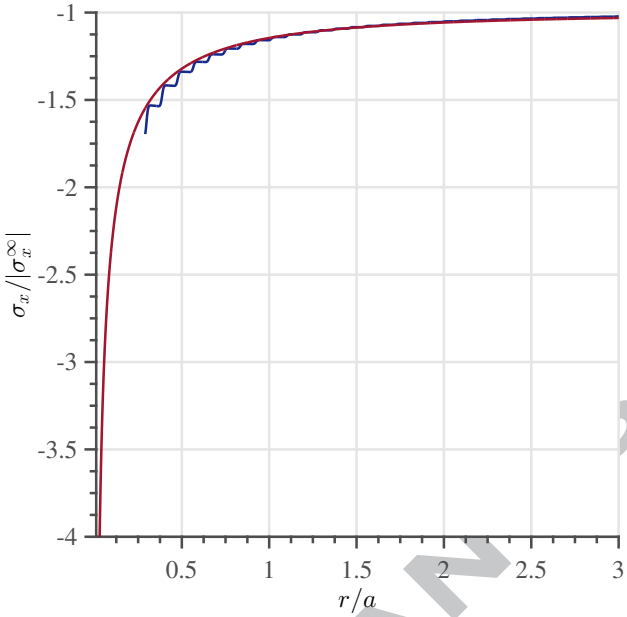

Figure 6: Numerical (continuous line) and analytical (dashed line) solutions (Atkinson, 1973) according to equation (6) for horizontal compressive loading

4.6. Mode I under biaxial loading

From the previous section, it emerged that an anticrack creates a singularity in the stress under any arbitrary biaxial loading, both tensile and compressive. However, this is true except in some circumstances. For instance, in plane strain for incompressible materials (equation (14)), for which $\kappa = 1$. For a compressible solid, K_I is null if $H_I = 0$, and, for equation (13), when $A = 0$. Hence, for equation (9), $A = 0$ for the following ratio between the loadings

$$\psi = \frac{\sigma_y^\infty}{\sigma_x^\infty} = -\frac{\kappa + 1}{\kappa - 3} \tag{63}$$

Figures 7 show that for this ratio there is no singularity, and that the inclusion is *transparent* to the applied load: the stress state in the matrix is uniform.

4.7. Inclined multiple rigid line inclusions in a soft matrix

To test the numerical method for large rotations of the RLI, the following examples assume an initially inclined anticrack within a very deformable matrix. The domain is stretched uni-axially. The matrix follows a compressible hyperelastic Neo-Hookean model. The choice of a compressible model stands in avoiding numerical issues related to incompressibility. There is quite a literature on the treatment of the incompressibility constraint in meshfree methods. However, the incompressibility issue is outside the scopes of the paper. This section wants to show that, under the assumption of finite deformation, the fibres rotate (and translate) in an evident manner. These results prove that the

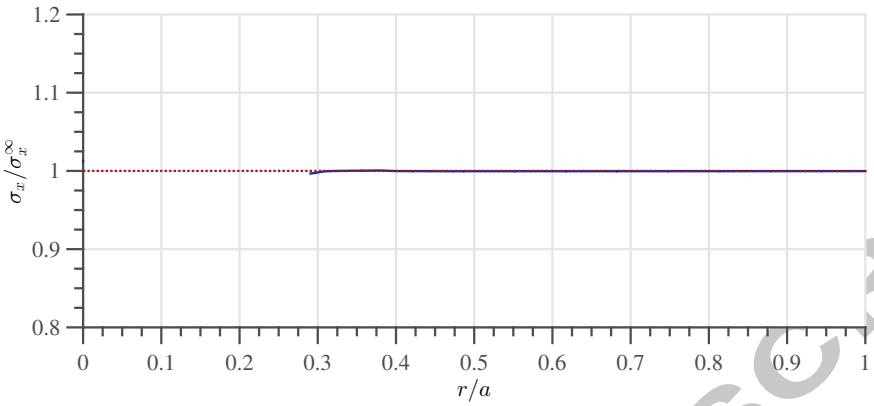

(a) σ_x

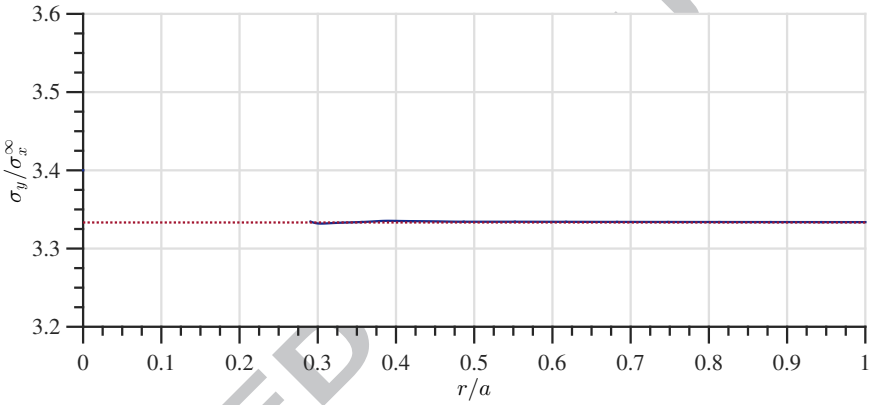

(b) σ_y

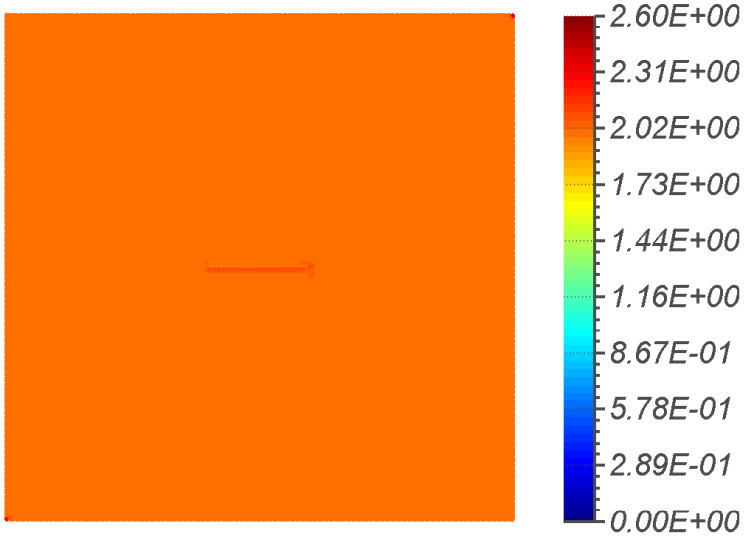

(c) Von Mises

Figure 7: Biaxial loading with ratio ψ in equation (63): Numerical (continuous line) and analytical (dashed line) solutions (Atkinson, 1973). Note that the singularity disappears, as evidenced by the horizontal lines (figures 7a and 7b) and by the uniform distribution (figure 7c)

method can capture the physical intuition. For example, it can reproduce the reorientation of inclined fibres towards the direction of loading, phenomenon important in many biological systems (Tower et al., 2002). The alignment of the fibres with the loading has structural importance since, in this manner, reinforcements can be the most effective in withstanding loads. The reorientation is facilitated if the matrix is compliant. The strain energy function W of the hyperelastic model is

$$W = \frac{1}{2}\mu_0 (I_1 - 3) + \lambda_0 \frac{1}{2} (\log J)^2 - \mu_0 \log J \tag{64}$$

where μ_0 is the *initial* shear modulus, λ_0 the *initial* bulk modulus, I_1 is the first invariant of the Right Cauchy Green tensor

$$\mathbf{C} = \mathbf{F}^T \mathbf{F} \tag{65}$$

The corresponding Second Piola-Kirchhoff Stress is

$$\mathbf{S} = \mu_0 \mathbf{I} - (\mu_0 - \lambda_0 \log J)\, \mathbf{C}^{-1} \tag{66}$$

The second elasticity tensor (in index notation) is

$$(\mathbb{C}_{SE})_{ijkl} = \lambda_0 C^{-1}_{ij} C^{-1}_{kl} + (\mu_0 - \lambda_0 \log J) \left(C^{-1}_{ik} C^{-1}_{jl} + C^{-1}_{il} C^{-1}_{kj} \right) \tag{67}$$

In the following examples, unless differently specified, $\mu_0 = 0.4$ MPa, with initial Poisson ratio of $\nu = 0.3$. The domain of study is the same as the previous sections (unit square of $L = 1$ m) under uniaxial stretch λ in the Y direction. The midpoint of the RLI is in the middle of the square.

4.7.1. One inclined anticrack: influence of large strains

The first series of results show the reorientation of the RLI under large values of λ. The length of the anticrack $2a$ is set to $L/10$, inclined with an angle β. The sample is discretized with a regular grid of 100×100 nodes, where the top and the bottom edges are clamped, and the top one free to move in the Y direction. The test is under *displacements-controlled* conditions, applied with an interval $\Delta\lambda = 0.02$. Figures in block 9 show the angle θ as a (non-linear) function of λ, and all the consequent deformations (translation and rotation) of a RLI with a slight initial inclination ($\beta = 15°$). Under a large finite strain of 400%, the RLI rotates of 55°. At $\lambda = 5$ the simulation halted for excessive localized deformation near the RLI, which brought J to be negative. As expected, the midpoint of the RLI (which is different from the center of rotation **c**) translates only vertically.

4.7.2. One inclined anticrack: influence of the initial angle

Figures in block 10 show the reorientation of RLIs with different initial inclination. As expected, under tension, the reorientation is less for RLIs with high initial inclination, while the reverse verifies for compressive loadings. In fact, for compressive strains of 30%, the anticrack at $\beta = 75°, 60°, 45°, 30°$ reorientate of nearly $-15°$. Some with a nonlinear variation ($\beta = 75°, 60°$), whilst the remaining with almost a linear law. Instead, the anticrack with $\beta = 15°$ reorientates of $-6°$.

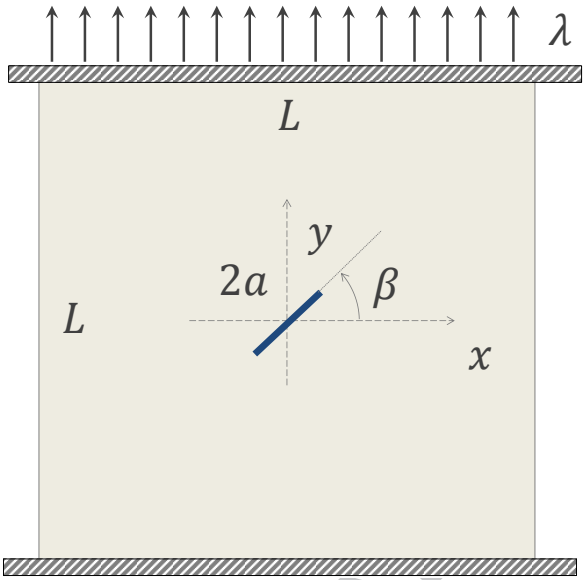

Figure 8: Anticrack in mixed-mode loading under a large uniaxial stretch

4.7.3. One inclined anticrack: influence of the initial stiffness

Figure 11 shows the influence of the stiffness of the matrix on the reorientation of the anticrack, as obtained from the numerical results. As intuitively expected, the same load can reorientate the RLI of a larger amount than a stiffer matrix: for example, for a load of 2 MPa, a 10 times stiffer matrix reorientates of 5°, instead of more than 20°. From a different point of view, a stiffer matrix requires a higher stress than a more compliant matrix to reorientate of the same quantity. A 10 times stiffer matrix requires a 10 times higher stress. This is justifiable also from a theoretical perspective, where under uniaxial stress, the Cauchy stress along the direction of loading is given by

$$\sigma_{22} = \frac{\mu_0}{J^{5/3}}\left(\lambda^2 - \frac{J}{\lambda}\right) \tag{68}$$

where J is obtained by solving the following nonlinear equation

$$\lambda_0\left(J^{8/3} - J^{5/3}\right) + \mu_0\left(\frac{J}{3\lambda} - \frac{\lambda^2}{3}\right) = 0 \tag{69}$$

Equations (68) and (69) are valid in absence of anticracks, or, for relatively small ones, far from them. It is evident from equation (69) that under uniaxial stress, different μ_0 (and hence λ_0) give the same J. Therefore, for equation (68) , σ_{22} is linearly proportional to the shear modulus.

4.7.4. One inclined anticrack: influence of the initial length

Figure 12 shows the effect of the length of the anticrack on the deformation of the matrix. The initial angle is $\beta = 15°$, with three different lengths, from relatively small, to the extreme case of an anticrack along the entire width.

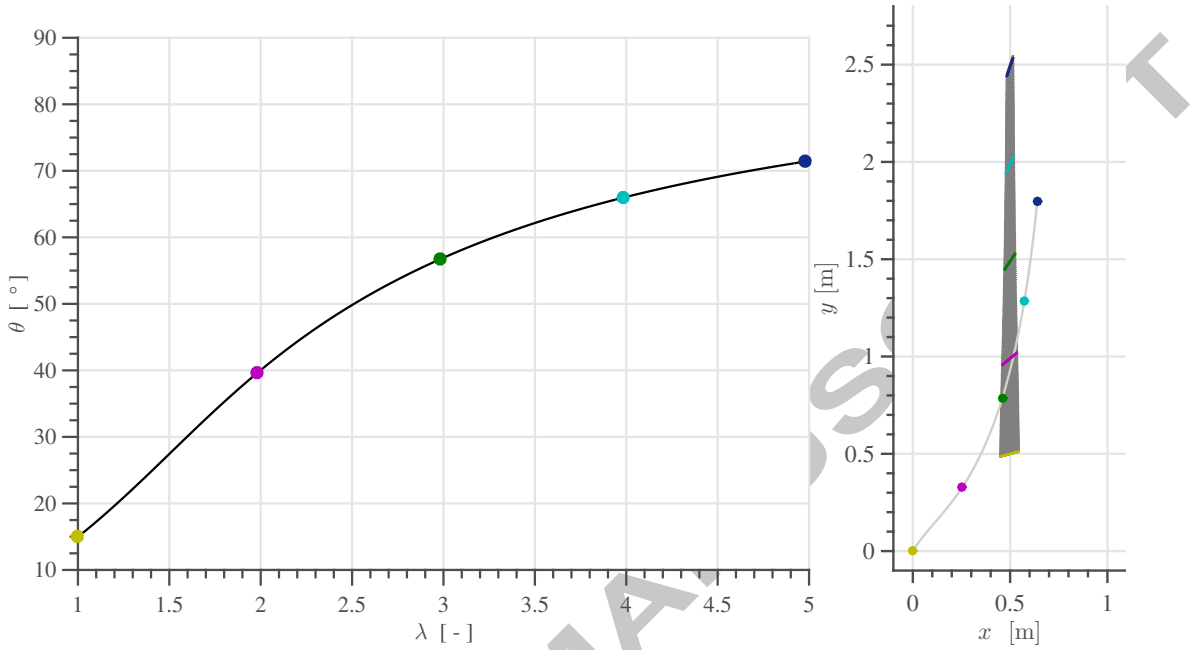

(a) Orientation of the RLI

(b) Trajectory of the center of rotation **c** (light grey), and deformation of the RLI (grey) as in equation (20)

Figure 9: Reorientation of a RLI with $\beta = 15°$ embedded in a soft matrix, under uniaxial stretch: dots are color-coded with a fixed value of λ

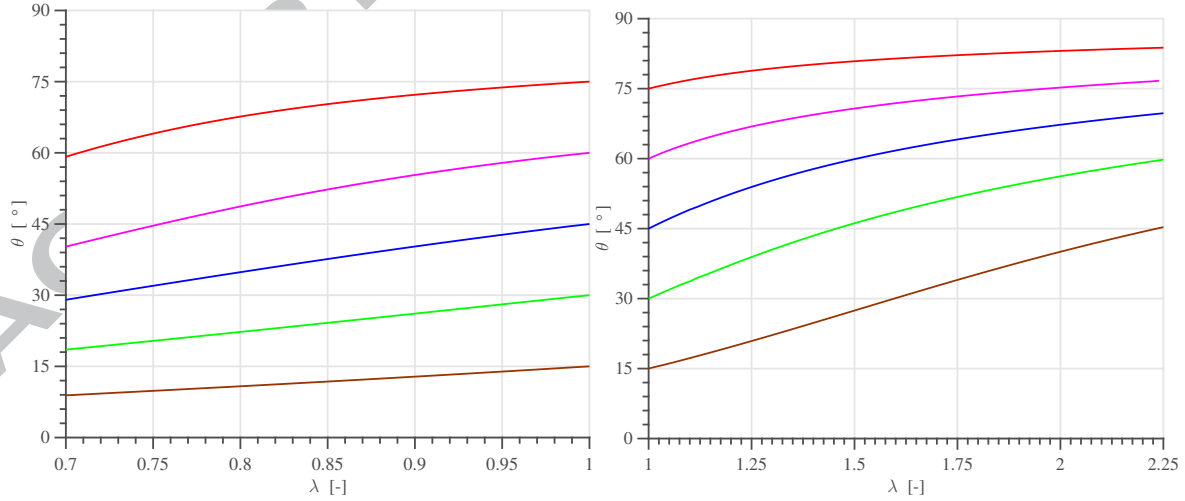

(a) Compressive stretch

(b) Tensile stretch

Figure 10: Reorientation of a RLI for different β; red: $\beta = 75°$; magenta: $\beta = 60°$; blue: $\beta = 45°$; green: $\beta = 30°$; brown: $\beta = 15°$;

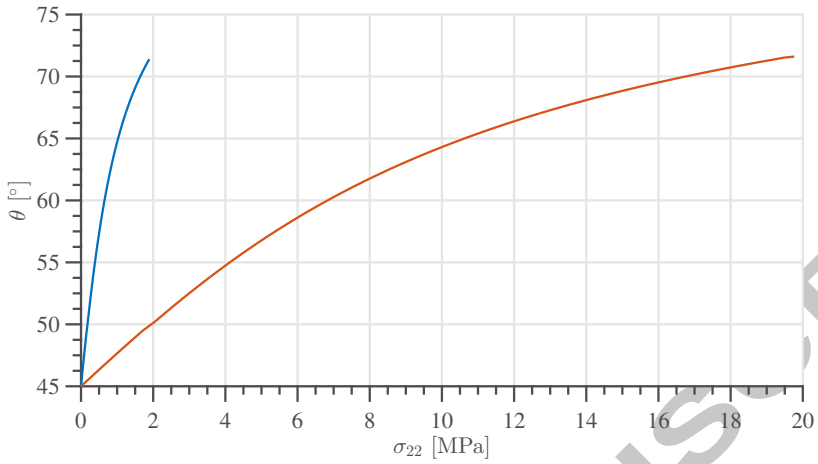

Figure 11: Influence of the initial stiffness (with the same initial ν); blue: $\mu_0 = 0.42$ MPa; red: $\mu_0 = 4.2$ MPa

Figure 12 is a zoom of the position of the anticrack and the deformation of the edges for $\lambda = 5$. There is no influence of the length on the final rotation and position of the anticrack. However, as the length augments, the RLI increasingly strains the matrix. In the extreme case, the edges deform by creating a kink.

4.7.5. Two inclined anticracks

This section examines the mutual influence of the inclined anticracks as depicted in figures 13. The centres of the two RLIs are separated by a distance $b = L/3$, with $2a = L/10$. Figure 14 shows the results of two different configurations: one with anticracks with equal inclination, and one with opposite. The colors of the curves are the same of the RLIs in figure 14. In both cases, for this value of b there is no influence on the rotation, and the two line inclusions deform as they were isolated, as reported in figure 10b (blue curve). To seek evidence for an interaction of the RLIs, the offset length b was reduced to half the length of the anticrack (a). Figure 15 displays only a slight difference in θ compared to figure 14a, and at large strains. The influence is the same also for RLIs inclined in an opposite direction (not reported). For anticracks, the local stress state near the tips does not seem to hinder significantly their reorientation.

4.7.6. Multiple RLIs

The last example considers a large number of randomly oriented anticracks. This case proves the power of the method, especially in handling multiple couplings between the matrix and the inclusions. It is useful to recall that *no remeshing* is necessary, and neither a mesh conforming to the anticrack lines: the distribution of nodes is a regularly arranged grid of 100×100 points. The test in figure 16 shows the reorientation of 49 anticracks. Their centers are regularly distributed, but their lengths and initial orientation are randomly chosen. The lengths are drawn from a uniform probability distribution function within an interval of $L/20$ and $L/15$; the initial angles instead from an interval of $\pi/4$ and $3/4\pi$. Once again, figures 16 and 17 show the realignment of the anticracks towards the direction

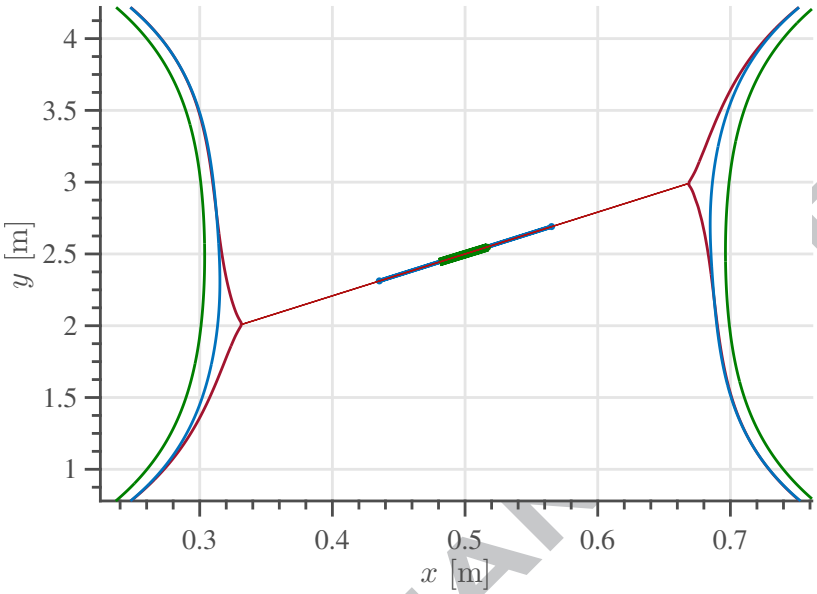

Figure 12: Influence of the initial length a, showing a detail of the final position of the anticrack (inclined straight lines) and the final deformation; green: $2a = L/10$; blue: $2a = 2/5L$; red: RLi along the width. Axes are rescaled for enhanced visualization.

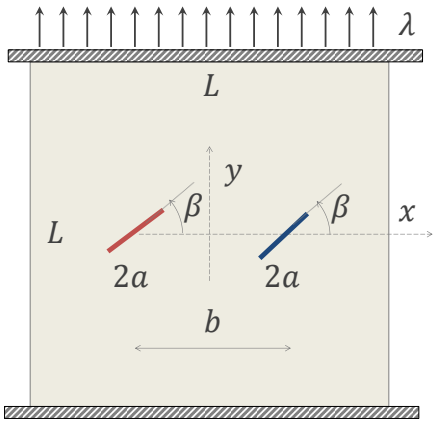

(a) Same initial inclination $\beta = 45°$

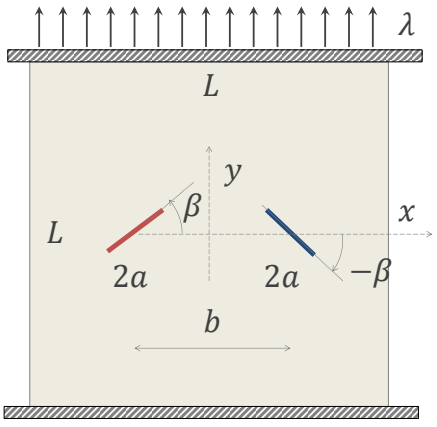

(b) Opposite initial inclination; red: $\beta = 45°$, blue $\beta = -45°$

Figure 13: Interaction of two anticracks: test cases and boundary conditions

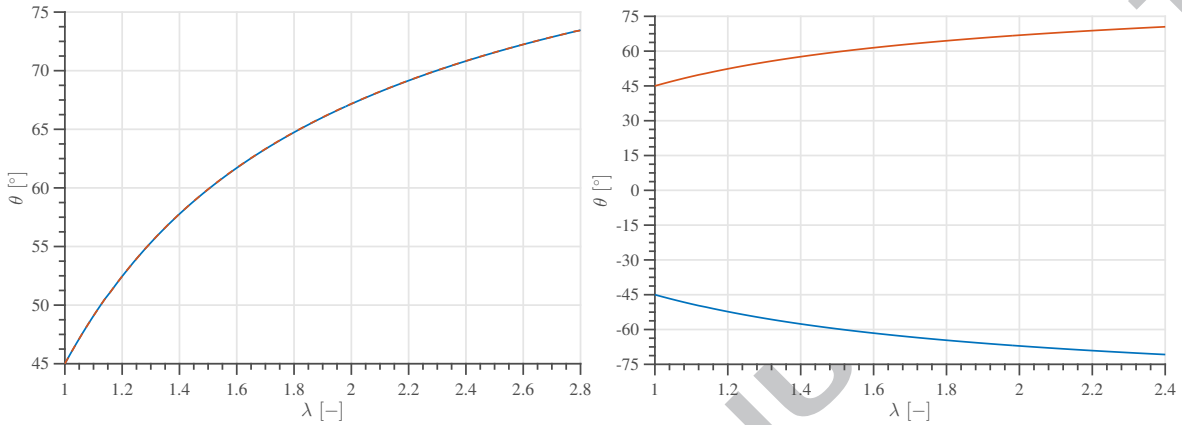

(a) Same initial inclination $\beta = 45°$

(b) Opposite initial inclination; red: $\beta = 45°$, blue $\beta = -45°$

Figure 14: Interaction of two anticracks: numerical results for $b = L/3$

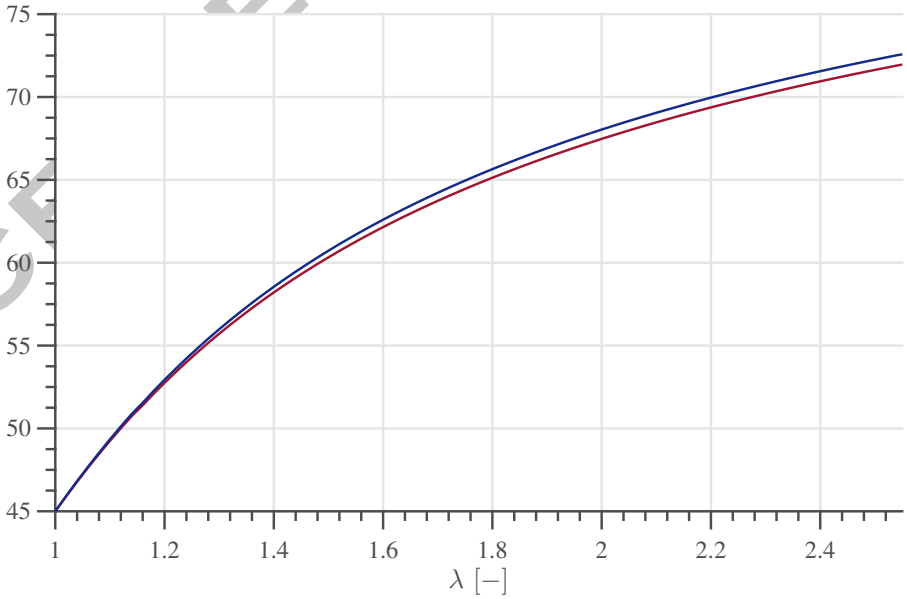

Figure 15: Interaction of two anticracks: numerical results for same initial inclination $\beta = 45°$ and $b = a$

of loading ($\pi/2$).

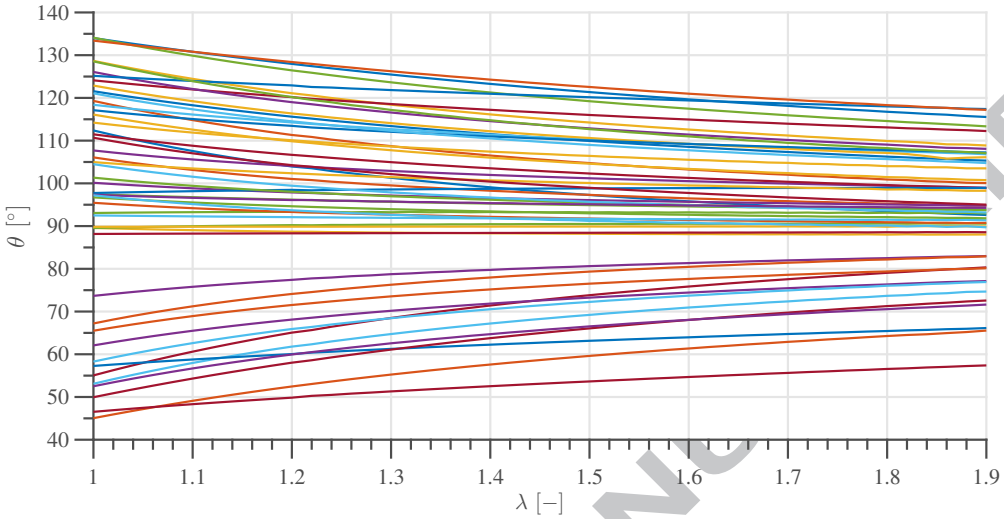

Figure 16: Reorientation of 49 randomly oriented anticracks

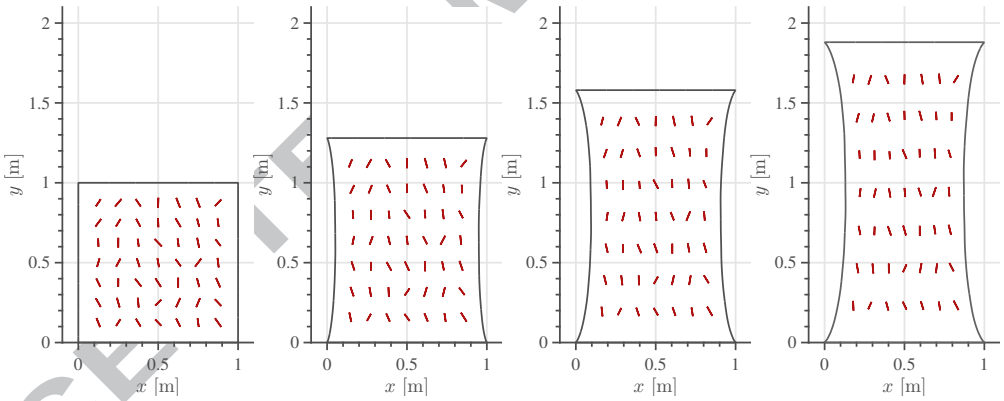

(a) $\lambda = 1.0$ (b) $\lambda = 1.3$ (c) $\lambda = 1.6$ (d) $\lambda = 1.9$

Figure 17: Deformed configuration of an hyperelastic matrix with 49 randomly oriented anticracks

4.8. Remarks on the nonlinear solution

Owing to the strong diagonal dominance of the tangent stiffness matrix in equation (55), the method converges rather quickly even for numerous anticracks. For the loads increments of $\delta\lambda = 0.02$, the solutions converged to a relative residual norm of 0.1% in only a couple of iterations. Even if a sophisticated nonlinear solver, like a *line search*, was available, this option was never activated, and a standard Newton-Rahpson solver sufficed. However, it is advisable to keep the increments short: for *large* increments, the solver might fail due to negative Jacobian.

5. Conclusions

This paper presented a numerical implementation of the *rigid line inclusion* model. A rigid line inclusion, also known as *anticrack*, *line stiffener*, *lamellar inhomogeneity* or *rigid ribbon*, is a kinematic model of a very thin and infinitely stiff reinforcement in an elastic matrix. Using numerical *meshfree* techniques for crack modelling, we presented a straightforward generalization that could prove to be useful for modelling engineered nanocomposites and hierarchical nano and microstructures occurring in natural systems. Linear elastic matrices were considered for ease of validation with existing analytical solutions; results showed rapid convergence to analytical stress intensity factors, for relatively coarse mesh sizes, and very good agreement (apart from the stress singularities) with the theoretical solutions given by (Atkinson, 1973). Differently from cracks, stress singularities appear also for compressive loadings normal to the inclusion, and for both tensile and compressive loadings parallel to the inclusion: instead, it is *transparent* for a certain combination of biaxial loadings, whose ratio can be predicted from the theory (Atkinson, 1973). The presented method is able to reproduce successfully all these peculiar characteristics of an anticrack. The method is extended easily to both nonlinear elasticity and to multiple anticracks. Both these cases are difficult to treat with analytical solutions and for general geometries. In fact, this paper presented results of one anticrack embedded in a soft matrix, modelled with an isotropic Neo-Hookean constitutive law. As an example, we considered a fibre-reorientation problem under large strains, common in many biological systems, and reported the orientation of the inclusion with respect to length, initial inclination and the stiffness of the matrix. Furthermore, we discussed the influence of two anticracks, and found that there is only slight influence (less than 1 degree) on the reorientation for very close RLIs. Finally, to prove the power of the approach, we presented an example with 49 anticracks, randomly oriented, and proved that such a complicated system requires no advanced meshing techniques for its treatment.

Appendix A. Numerical computation of the *J*-integral

Following (Li et al., 1985), the *J*-integral (Rice, 1968) for single mode loading and a crack that grows straight ahead can be re-formulated as in equation (15), where A is the domain enclosed by a closed curve Γ oriented anti-clockwise that surrounds the crack tip $\mathbf{x}_c$, q is a weight function that is zero on Γ and 1 on $\mathbf{x}_c$ (Fig. A.18), W is the *strain energy density* that for a linear elastic material can be written as

$$W = \frac{1}{2}\boldsymbol{\sigma} : \boldsymbol{\epsilon} \tag{A.1}$$

The chosen weight function (Fig. A.18) is an asymmetric *hat* function given by

$$\begin{aligned} w(x,y) &= w_x(x)w_y(y) \\ w_x(x) &= \left[\mathcal{H}(x+d_x^l) - \mathcal{H}(x)\right]\frac{x+d_x^l}{d_x^l} + \left[\mathcal{H}(x) - \mathcal{H}(x-d_x^r)\right]\frac{-x+d_x^r}{d_x^r} \\ w_y(y) &= \left[\mathcal{H}(y+d_y^l) - \mathcal{H}(y)\right]\frac{y+d_y^l}{d_y^l} + \left[\mathcal{H}(y) - \mathcal{H}(y-d_y^r)\right]\frac{-y+d_y^r}{d_y^r} \end{aligned} \tag{A.2}$$

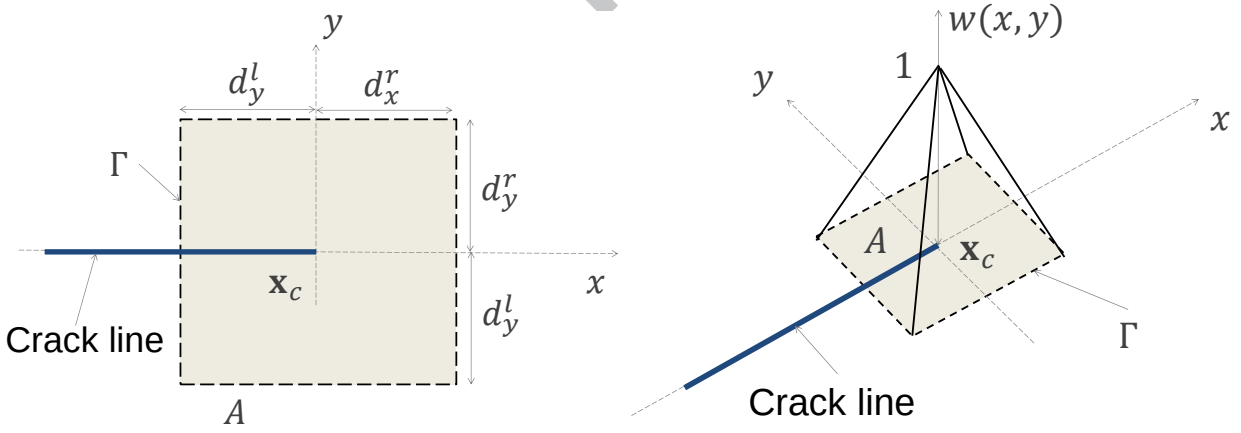

(a) Coordinate reference system (b) Weight function

Figure A.18: Domain and weight function w for the *J*-integral

Acknowledgements

NMP is supported by the European Research Council (ERC StG Ideas 2011 BIHSNAM n. 279985 on Bio-Inspired hierarchical super-nanomaterials, ERC PoC 2013-1 REPLICA2 n. 619448 on Large-area replication of biological anti-adhesive nanosurfaces, ERC PoC 2013-2 KNOTOUGH n. 632277 on Super-tough knotted fibres), by the European Commission under the Graphene Flagship (WP10 "Nanocomposites", n. 604391) and by the Provincia

Autonoma di Trento ("Graphene Nanocomposites", n. S116/2012-242637 and reg.delib. n. 2266). EB is supported by the Queen Mary University of London Start-up grant for new academics.

References

Atkinson, C., 1973. Some ribbon-like inclusion problems. International Journal of Engineering Science 11 (2), 243–266.

Ballarini, R., 1987. An integral equation approach for rigid line inhomogeneity problems. International Journal of Fracture 33 (2), R23–R26.

Ballarini, R., 1990. A rigid line inclusion at a bimaterial interface. Engineering Fracture Mechanics 37 (1), 1–5.

Barbieri, E., Meo, M., 2012. A fast object-oriented matlab implementation of the reproducing kernel particle method. Computational Mechanics 49 (5), 581–602.

Barbieri, E., Petrinic, N., 2013a. Multiple crack growth and coalescence in meshfree methods with a distance function-based enriched kernel. In: Key Engineering Materials - Advances in Crack Growth Modeling. TransTech Publications, p. 170.

Barbieri, E., Petrinic, N., 2013b. Three-dimensional crack propagation with distance-based discontinuous kernels in meshfree methods. Computational Mechanics, 1–18.

Barbieri, E., Petrinic, N., Meo, M., Tagarielli, V., 2012. A new weight-function enrichment in meshless methods for multiple cracks in linear elasticity. International Journal for Numerical Methods in Engineering 90 (2), 177–195.

Belytschko, T., Liu, W. K., Moran, B., 2000. Nonlinear finite elements for continua and structures. John Wiley & Sons.

Bigoni, D., Dal Corso, F., Gei, M., 2008. The stress concentration near a rigid line inclusion in a prestressed, elastic material. part ii.: Implications on shear band nucleation, growth and energy release rate. Journal of the Mechanics and Physics of Solids 56 (3), 839–857.

Bilotti, E., Deng, H., Zhang, R., Lu, D., Bras, W., Fischer, H. R., Peijs, T., 2010. Synergistic reinforcement of highly oriented poly (propylene) tapes by sepiolite nanoclay. Macromolecular Materials and Engineering 295 (1), 37–47.

Bilotti, E., Fischer, H., Peijs, T., 2008. Polymer nanocomposites based on needle-like sepiolite clays: Effect of functionalized polymers on the dispersion of nanofiller, crystallinity, and mechanical properties. Journal of Applied Polymer Science 107 (2), 1116–1123.

Bilotti, E., Zhang, R., Deng, H., Quero, F., Fischer, H., Peijs, T., 2009. Sepiolite needle-like clay for pa6 nanocomposites: An alternative to layered silicates? Composites Science and Technology 69 (15-16), 2587–2595.

Brussat, T., Westmann, R., 1975. A westergaard-type stress function for line inclusion problems. International Journal of Solids and Structures 11 (6), 665–677.

Burnley, P., Green, H., 1989. Stress dependence of the mechanism of the olivine-spinel transformation. Nature 338, 753–756.

Chen, Y., 1986. Singular behaviour at fixed rigid line tip in plane elasticity. Engineering fracture mechanics 25 (1), 11–16.

Dal Corso, F., Bigoni, D., 2009. The interactions between shear bands and rigid lamellar inclusions in a ductile metal matrix. Proceedings of the Royal Society A: Mathematical, Physical and Engineering Science 465 (2101), 143–163.

Dal Corso, F., Bigoni, D., Gei, M., 2008. The stress concentration near a rigid line inclusion in a prestressed, elastic material. part i.: Full-field solution and asymptotics. Journal of the Mechanics and Physics of Solids 56 (3), 815–838.

Dundurs, J., Markenscoff, X., 1989. A green's function formulation of anticracks and their interaction with load-induced singularities. Journal of applied mechanics 56 (3), 550–555.

Eichhorn, S., Dufresne, A., Aranguren, M., Marcovich, N., Capadona, J., Rowan, S., Weder, C., Thielemans, W., Roman, M., Renneckar, S., et al., 2010. Review: current international research into cellulose nanofibres and nanocomposites. Journal of Materials Science 45 (1), 1–33.

Fletcher, R. C., Pollard, D. D., 1981. Anticrack model for pressure solution surfaces. Geology 9 (9), 419–424.

Fratzl, P., Guille, M. M. G., 2011. Hierarchy in natural materials. Hierarchically Structured Porous Materials.

Green, H. W., Young, T. E., Walker, D., Scholz, C. H., 1990. Anticrack-associated faulting at very high pressure in natural olivine. Nature 348 (6303), 720–722.

Hasebe, N., Keer, L., Nemat-Nasser, S., 1984. Stress analysis of a kinked crack initiating from a rigid line inclusion. part 1: Formulation. Mechanics of Materials 3 (2), 131–145.

Heierli, J., Gumbsch, P., Zaiser, M., 2008. Anticrack nucleation as triggering mechanism for snow slab avalanches. Science 321 (5886), 240–243.

Hurtado, J., Dundurs, J., Mura, T., 1996. Lamellar inhomogeneities in a uniform stress field. Journal of the Mechanics and Physics of Solids 44 (1), 1–21.

Ji, B., Gao, H., 2004. Mechanical properties of nanostructure of biological materials. Journal of the Mechanics and Physics of Solids 52 (9), 1963–1990.

Landis, W., 1995. The strength of a calcified tissue depends in part on the molecular structure and organization of its constituent mineral crystals in their organic matrix. Bone 16 (5), 533–544.

Li, F., Shih, C., Needleman, A., 1985. A comparison of methods for calculating energy release rates. Engineering Fracture Mechanics 21 (2), 405–421.

Liu, W., Jun, S., Zhang, Y., 1995. Reproducing kernel particle methods. International journal for numerical methods in fluids 20 (8-9), 1081–1106.

Muskhelishvili, N. I., 1953. Some basic problems of the mathematical theory of elasticity. Vol. 15. Cambridge Univ Press.

Nishimura, N., Liu, Y., 2004. Thermal analysis of carbon-nanotube composites using a rigid-line inclusion model by the boundary integral equation method. Computational Mechanics 35 (1), 1–10.

Noselli, G., Dal Corso, F., Bigoni, D., 2010. The stress intensity near a stiffener disclosed by photoelasticity. International journal of fracture 166 (1-2), 91–103.

Pingle, P., Sherwood, J., Gorbatikh, L., 2008. Properties of rigid-line inclusions as building blocks of naturally occurring composites. Composites science and technology 68 (10), 2267–2272.

Porwal, H., Grasso, S., Reece, M., 2013a. Review of graphene-ceramic matrix composites. Advances in Applied Ceramics 112 (8), 443–454.

Porwal, H., Tatarko, P., Grasso, S., Hu, C., Boccaccini, A. R., Dlouhỳ, I., Reece, M. J., 2013b. Toughened and machinable glass matrix composites reinforced with graphene and graphene-oxide nano platelets. Science and Technology of Advanced Materials 14 (5), 055007.

Porwal, H., Tatarko, P., Grasso, S., Khaliq, J., Dlouhỳ, I., Reece, M. J., 2013c. Graphene reinforced alumina nano-composites. Carbon 64, 359–369.

Radtke, F., Simone, A., Sluys, L., 2010. A partition of unity finite element method for obtaining elastic properties of continua with embedded thin fibres. International Journal for Numerical Methods in Engineering 84 (6), 708–732.

Radtke, F., Simone, A., Sluys, L., 2011. A partition of unity finite element method for simulating non-linear debonding and matrix failure in thin fibre composites. International Journal for Numerical Methods in Engineering 86 (4-5), 453–476.

Rice, J. R., 1968. A Path Independent Integral and the Approximate Analysis of Strain Concentration by Notches and Cracks. Journal of Applied Mechanics 35, 379–386.

Stagni, L., 1989. Line singularity near the tip of a crack and of a fixed rigid line: unified treatment. Engineering fracture mechanics 33 (5), 679–684.

Tower, T. T., Neidert, M. R., Tranquillo, R. T., 2002. Fiber alignment imaging during mechanical testing of soft tissues. Annals of biomedical engineering 30 (10), 1221–1233.

Walters, M. C., Paulino, G. H., Dodds, R. H., 2005. Interaction integral procedures for 3-d curved cracks including surface tractions. Engineering fracture mechanics 72 (11), 1635–1663.

Wang, Z., Zhang, H., Chou, Y., 1985. Characteristics of the elastic field of a rigid line inhomogeneity. Journal of applied mechanics 52 (4), 818–822.

1. For the first time, it is presented a numerical method that couples 2D matrices with exactly 1D (line, zero-thickness) inclusions, also named anticracks
2. The method matches available analytical solutions for simple cases, and in the linear elastic approximation.
3. The paper, in addition, presents an extension to soft matrices, modelled with hyperelastic laws, and with multiple line inclusions
4. The results show that the method capture the phenomenon of fibre reorientation towards the direction of loading